Recent Changes in the Atmospheric Circulation Patterns during the Dry-to-Wet Transition Season in South Tropical South America (1979-2020): Impacts on Precipitation and Fire Season

Jhan-Carlo Espinoza, Paola A Arias, Vincent Moron, Clementine Junquas, Hans Segura, Juan Pablo Sierra-Pérez, Sly Wongchuig, Thomas Condom, Juan Pablo Sierra-Pérez

Recent Changes in the Atmospheric Circulation Patterns during the Dry-to-Wet Transition Season in South Tropical South America (1979–2020): Impacts on Precipitation and Fire Season

JHAN-CARLO ESPINOZA,[a] PAOLA A. ARIAS,[b] VINCENT MORON,[c,d] CLEMENTINE JUNQUAS,[a] HANS SEGURA,[a] JUAN PABLO SIERRA-PÉREZ,[a] SLY WONGCHUIG,[a] AND THOMAS CONDOM[a]

[a] *Institut des Géosciences de l'Environnement, Université Grenoble Alpes, IRD, CNRS, Grenoble, France*
[b] *Grupo de Ingeniería y Gestión Ambiental, Escuela Ambiental, Facultad de Ingeniería, Universidad de Antioquia, Medellín, Colombia*
[c] *Aix-Marseille University, CNRS, IRD, INRAE, Collège de France CEREGE, Aix-en-Provence, France*
[d] *International Research Institute for Climate and Society, Lamont-Doherty Earth Observatory, Columbia University, Palisades, New York*

(Manuscript received 17 April 2021, in final form 3 July 2021)

ABSTRACT: We analyze the characteristics of atmospheric variations over tropical South America using the pattern recognition framework of weather typing or atmospheric circulation patterns (CPs). During 1979–2020, nine CPs are defined in the region, using a *k*-means algorithm based on daily unfiltered 850-hPa winds over 10°N–30°S, 90°–30°W. CPs are primarily interpreted as stages of the annual cycle of the low-level circulation. We identified three "winter" CPs (CP7, CP8, and CP9), three "summer" CPs (CP3, CP4, and CP5), and three "transitional" CPs (CP1, CP2, and CP6). Significant long-term changes are detected during the dry-to-wet transition season (July–October) over southern tropical South America (STSA). One of the wintertime patterns (CP9) increases from 20% in the 1980s to 35% in the last decade while the "transitional" CP2 decreases from 13% to 7%. CP9 is characterized by enhancement of the South American low-level jet and increasing atmospheric subsidence over STSA. CP2 is characterized by southerly cold-air incursions and anomalous convective activity over STSA. The years characterized by high frequency of CP9 and low frequency of CP2 during the dry-to-wet transition season are associated with a delayed South American monsoon onset and anomalous dry conditions over STSA. Consistently, a higher frequency of CP9 intensifies the fire season over STSA (1999–2020). Over the Brazilian states of Maranhão, Tocantins, Goiás, and São Paulo, the seasonal frequency of CP9 explains around 35%–44% of the interannual variations of fire counts.

KEYWORDS: Amazon region; South America; Atmospheric circulation; Interannual variability; Subseasonal variability; Trends

1. Introduction

The South American monsoon system (SAMS) is an important feature of the seasonal rainfall variations in southern tropical South America (STSA; 5°–25°S, 40°–80°W). Over this region, more than 50% of the total annual rainfall is reported during the active phase of the SAMS, usually observed during the austral summer (December–February) (Zhou and Lau 1998; Vera et al. 2006; Marengo et al. 2012). Consequently, the SAMS plays a major role in the regulation of the water cycle over STSA, contributing in the maintenance of ecosystems and human activities (e.g., Fu et al. 2013; Brando et al. 2014; Nobre et al. 2016; Arias et al. 2020). Precipitation related to the monsoonal circulation of the SAMS mainly affects areas of Bolivia, Peru, Brazil, and northern Argentina, covering the southern part of the Amazon rain forest and the Cerrado biome (e.g., Garreaud 2009; Espinoza et al. 2009, 2020; Correa et al. 2021). Four dominant atmospheric features have been involved in the SAMS: (i) warmer sea surface temperatures (SSTs) over the tropical Atlantic Ocean and cooler surface temperature in southern Amazonia preceding the wet-season onset; (ii) a northwest–southeast band of convergence and convective activity over the southeast of the continent [the South Atlantic convergence zone (SACZ)]; (iii) an upper troposphere anticyclone (at 200–300 hPa), located over Bolivia, known as the Bolivian high; and (iv) the presence of a low-level jet to the east of the tropical Andes, known as the South American low-level jet (SALLJ). These ocean–atmospheric mechanisms have been reviewed and analyzed in previous studies (e.g., Lenters and Cook 1997; Fu et al. 1999; Gan et al. 2004; Vera et al. 2006; da Silva and de Carvalho 2007; Garreaud et al. 2009; Marengo et al. 2012; Yin et al. 2014; Arias et al. 2015; Green et al. 2020).

In the past decades, significant efforts have been dedicated to identifying processes that control the onset of the SAMS around September–October. The reversal of the cross-equatorial low-level flow, from a southerly to a northerly regime, is an important mechanism for the atmospheric moisture transport from the northern tropical Atlantic Ocean to STSA (Wang and Fu 2002; Li and Fu 2004). For instance, the increase in the frequency of the cross-equatorial northerly winds during austral spring (September–November) is associated with the onset of the wet season in northwestern Amazonia (Wang and Fu 2002). In addition, different studies also suggested that the increase of latent heat and surface moisture fluxes, related to tree transpiration, contributes

Supplemental information related to this paper is available at the Journals Online website: https://doi.org/10.1175/JCLI-D-21-0303.s1.

Corresponding author: Jhan-Carlo Espinoza, jhan-carlo.espinoza@ird.fr

DOI: 10.1175/JCLI-D-21-0303.1

much of the water for rainfall over this region (e.g., Fu and Li 2004; Wright et al. 2017).

Considering different regions over tropical South America and using different methods (mainly based on convective activity and precipitation), several studies have characterized the onset and demise dates of the SAMS [see Correa et al. (2021) for a comparative analysis]. In relation to an increase of dry conditions in southern Amazonia during the dry-to-wet transition season (e.g., Espinoza et al. 2019a,b; Funatsu et al. 2021), studies have documented a significant delay in the SAMS onset and lengthening of the dry season in STSA in recent decades (e.g., Fu et al. 2013; Arias et al. 2015; Debortoli et al. 2015; Arvor et al. 2017; Agudelo et al. 2019; Giráldez et al. 2020; Haghtalab et al. 2020; Correa et al. 2021). For example, Fu et al. (2013) estimated a lengthening of the dry season over the southern Amazonia of about 6.5 ± 2.5 days per decade for the period 1979–2011. The authors suggested that the delayed SAMS onsets are associated with a poleward shift of the subtropical jet over South America and an increase in the convective inhibition (CIN) during the austral winter (June–August). In addition, Arias et al. (2015) showed that anomalously warm SST in the tropical North Atlantic Ocean, the positive phase of the Atlantic multidecadal oscillation (AMO), and the El Niño events are associated with the delay of the SAMS onset reported during the last four decades. For instance, during the 2015/16 El Niño–related drought, the onset of the rainy season over the central Amazonia in 2015 occurred 10–15 days later than the normal onset date (Marengo et al. 2017). In accordance with these results, studies identified that variations of SSTs over the Pacific (e.g., El Niño or La Niña events) and positive or negative SST anomalies in the Atlantic Ocean are related to interannual rainfall variability in the Amazonian region (e.g., Liebmann and Marengo 2001; Arvor et al. 2017; Espinoza et al. 2019a; Jimenez et al. 2021). In particular, the rainfall decrease observed throughout the last four decades in southern Amazonia during the dry-to-wet transition season has been associated with an increased atmospheric subsidence over this region as part of the intensification of the Hadley and Walker cells (e.g., Yoon and Zeng 2010; Arias et al. 2015; Espinoza et al. 2016, 2019a; Barichivich et al. 2018; Agudelo et al. 2019; Segura et al. 2020). On the other hand, recent studies also show that delays of the SAMS onset are influenced by anthropogenic forcing, such as deforestation and related changes in the regional hydrological cycle (Butt et al. 2011; Debortoli et al. 2015; Wright et al. 2017, Ruiz-Vásquez et al. 2020).

In relation to the above-described lengthening of the dry season in the southern Amazon, several studies have documented a decline of Amazon biomass during the last decades (e.g., Brienen et al. 2015). In particular, a higher frequency of extreme droughts in the southern Amazon (Marengo and Espinoza 2016) promoted an anomalously extensive and severe fire season over this region (Brando et al. 2014; Alencar et al. 2015; Aragão et al. 2018; Libonati et al. 2021). For instance, during the dry seasons of 2005, 2007, 2010, and 2015/16, high biomass burning in the southern Amazon and Brazilian Cerrado were reported (Fernandes et al. 2011; Chen et al. 2017; Libonati et al. 2021). In addition to climate variability, deforestation has been recognized as a key driver of vegetation burning in Amazonia, which is enhanced during extreme droughts and periods of weak forest governance (Barlow et al. 2020; Staal et al. 2020). While most studies have documented the role of the large-scale climatic factors at interannual time scale on the intensity of fire season (e.g., El Niño and anomalously warm SSTs in the Atlantic Ocean), little is known about intraseasonal atmospheric circulation regimes that could promote fire activities in tropical South America. In addition, the internal dynamics of the atmosphere exhibits a broad spectrum of motions, primarily dominated by the annual cycle; however, changes in characteristics atmospheric regimens during the dry-to-wet transition season on STSA can provide additional information about the role of large-scale climate variability on the lengthening of the SAMS onset and its related impacts on fire activity. Under this context, the improvement of our understanding about the atmospheric circulation patterns related to changes in the SAMS onset and the consequent lengthening of the dry season in STSA remains a high-priority issue from a scientific and societal point of view. In this study, we investigate the daily atmospheric circulation regimes during the dry-to-wet transition season in STSA using the pattern recognition framework of weather typing or atmospheric circulation patterns (CPs).

Weather types or CPs are usually defined as recurrent and potentially predictable atmospheric situations, which can be related to dependent local variables such as rainfall or temperature (Hewitson and Crane 2002; Solman and Menéndez 2003; Moron et al. 2008; Bettolli et al. 2010). In this study, CPs will be related to atmospheric mechanisms associated with changes in the SAMS onset and lengthening of the dry season in STSA. Two complementary approaches are used to evaluate atmospheric variability, with or without explicit time filtering. Applying a temporal filter in atmospheric data (e.g., removing the annual cycle or interannual variability) has the advantage of focusing on a specific time scale, thus emphasizing the impact of some particular climatic phenomena. However, this approach has the potential disadvantage that could be detrimental due to potential aliasing between time scales and removing the largest fraction of temporal variance due to the annual cycle of solar radiation. In tropical South America, this method has been used by Espinoza et al. (2012, 2013, 2015), da Anunciação et al. (2014), Paccini et al. (2018), and Figueroa et al. (2020) to analyze the relationship between intraseasonal atmospheric circulation and high-frequency hydroclimatic events, such as extreme rainy days and impacts on river water levels, dry spells, and cold surges. Another approach is the CP definition based on atmospheric variables without any time filtering. This approach considers all bandwidths including the annual cycle together with intra- and interannual variations. Thus, the partitioning in CPs is used as a coarse-grained statistical approach for analyzing atmospheric circulation covering, in theory, all time scales from daily up to the number of years included in the analysis (Ghil and Robertson 2002; Moron et al. 2010, 2016; Sáenz and Durán-Quesada 2015). This comprehensive approach is especially relevant for the characterization of transitional periods, such as the dry-to-wet one, when the main shift of the annual cycle is superimposed to other faster (intraseasonal and synoptic) and slower (interannual) time scales

(Moron et al. 2015; Gouirand et al. 2020). Applying the CP framework, without any time filtering, this study has three main goals: (i) to identify the CPs throughout the year, particularly those that are characteristic of the dry-to-wet transition over STSA; (ii) to analyze the temporal evolution of the CPs characteristics of the dry-to-wet transition season during the 1979–2020 period, in relation to the delayed SAMS onsets; and (iii) to analyze the impact of characteristic dry-to-wet transition season CPs on fire activities in STSA. Section 2 presents the data and methods used in this study. The main results are detailed and discussed in section 3, and the conclusions and final remarks are given in section 4.

2. Data and methods

a. Atmospheric data

To define the CPs, we use both zonal and meridional daily winds at 850 hPa in the region defined by 10°N–30°S, 90°–30°W for the 1979–2020 period, from the European Centre for Medium-Range Weather Forecasts (ECMWF) reanalysis ERA5 (Hersbach et al. 2020) dataset. In addition, zonal and meridional wind and vertical motion (vertical velocity) at pressure levels between 1000 and 100 hPa from the ERA5 reanalysis are also analyzed in relation to each CP. Convective inhibition from ERA5 is also analyzed as an indicator of the amount of energy preventing an air parcel to rise from the surface to the level of free convection. This new generation reanalysis of the ECMWF is available at a horizontal resolution of 0.28° × 0.28° (31 km) at hourly time step. In this study, daily data are used. These data are available online (https://www.ecmwf.int/en/forecasts/datasets/reanalysis-datasets/era5).

b. Outgoing longwave radiation and deep convective clouds datasets

To analyze deep convection, interpolated daily outgoing longwave radiation (OLR) from the NOAA dataset (hereinafter OLR-NOAA; Liebmann and Smith 1996) is used for the same space and time windows over South America. OLR-NOAA data at 2.5° of horizontal resolution are available at https://psl.noaa.gov/data/gridded/data.interp_OLR.html. OLR-NOAA data are used to define the onset of the South American monsoon system (as explained in section 2f). To complement this analysis, we also use OLR and information of cloud properties data from two products part of the Clouds and the Earth's Radiant Energy System (CERES) project. This project, launched in 2000, measures the energy fluxes at the top-of-the-atmosphere (TOA) and allows the study of global energy balance, cloud feedbacks and cloud properties (Wielicki et al. 1996). The CERES synoptic 1° (SYN1deg) daily means, edition 4.1, product is used in this work for analyzing TOA longwave radiation flux (hereinafter OLR-CERES). On the other hand, we use CERES Single Scanner Footprint (SSF)-level 3 product to identify the number of days with deep convective clouds for the July–October season (Doelling et al. 2013). These datasets present a horizontal resolution of 1° × 1°, cover the period 2000–20, and are available online (https://ceres.larc.nasa.gov/data/). For both products, the edition 4.1 is used. This version incorporates higher time resolution data and additional infrared channels than previous versions, improving the accuracy of high-temporal-resolution fluxes reducing longwave flux biases (Doelling et al. 2016). Following the method developed by Xu et al. (2016), we distinguish deep convective clouds based on a set of physically defined criteria. First, deep convective clouds are characterized by a cloud-top pressure between 440 and 50 hPa. Additionally, the cloud visible optical depth gives information about the level of transparency of different types of clouds. In this sense, higher values of the optical depth in the visible spectrum imply more scattering due to ice crystals and water droplets. For this reason, whereas optical depth values that are greater or equal than 10 are characteristic of thick deep convective clouds, smaller values are related to thinner clouds such as cirrus or cirrocumulus. As a final condition, more than 99% of the pixel area needs to be covered by clouds (cloud fraction > 0.99) (Xu et al. 2016). Grid cells for which these three conditions are accomplished are labeled as areas with deep convective clouds.

c. Precipitation datasets

In this study, we analyze the daily Climate Hazards Group Infrared Precipitation with Stations (CHIRPS) dataset, which combines satellite and rain gauge data (Funk et al. 2015). This rainfall dataset uses the global cold cloud duration (CCD), as a thermal infrared method to estimate the global precipitation. Then, the product TRMM-3B42 V7 is used to calibrate the precipitation estimated by the global CCD. Last, meteorological stations are utilized to calibrate the estimations of precipitation. The high spatial resolution (0.05° × 0.05°) and the temporal coverage from January 1981 to December 2020 make CHIRPS a suitable satellite precipitation product to study the precipitation variability over tropical South America, as shown in previous studies (Paccini et al. 2018; Espinoza et al. 2019a; Arias et al. 2020; Calvalcante et al. 2020; Paca et al. 2020; Funatsu et al. 2021). The CHIRPS V2.0 dataset is available online (https://data.chc.ucsb.edu/products/CHIRPS-2.0/global_daily/).

d. Active fire counts

The estimation of the active fire counts is based on the Brazilian national program "Programa Queimadas" from the National Institute for Space Research (INPE) of Brazil. The active fire counts detection is done through automatic processing of images obtained from nine satellites: *Terra, Aqua, Suomi NPP, NOAA-15, NOAA-18, NOAA-19, MetOp-B*, *GOES-16*, and *Meteosat-10* (*MSG-3*) (INPE 2018). The dataset used in this study is the last version, which includes the adoption of the algorithm and active fire detection data from MODIS Collection 6 and the correction of MODIS-detected fire pixels, based on the *Aqua* daily sensor at 1-km resolution. This dataset is produced by the INPE and is available from 1998 to the present (INPE 2018). Therefore, this information is fully compatible and integrated with the NASA MODIS Collection-6 fire product (Giglio et al. 2018; Libonati et al. 2021). In this study, monthly data averaged over the Brazilian states of Maranhão, Tocantins, Goiás, and São Paulo are analyzed. This dataset is available online (http://queimadas.dgi.inpe.br/queimadas/portal).

e. Definition of large-scale circulation patterns

Rather than giving technical details for the *k*-means method, which can be found in previous studies (e.g., Diday and Simon 1976;

Michelangeli et al. 1995; Straus and Molteni 2004; Sáenz and Durán-Quesada 2015), we provide here a broad picture of the overall method used for defining circulation patterns (CPs). Daily CPs are extracted from horizontal 850-hPa daily winds over the 10°N–30°S, 90°–30°W region and then clustered using a *k*-means dynamical algorithm (Michelangeli et al. 1995; Diday and Simon 1976) without any time filtering (e.g., Moron et al. 2015, 2016). The 850-hPa daily winds are first standardized at each ERA5 grid point using the long-term mean and standard deviation. This approach provides a large-scale overview of the atmospheric variability by considering, a priori, all time scales from daily to decadal. No significant changes in CPs are identified using other boundaries into STSA (e.g., 5°N–25°S or 5°–25°S).

The *k*-means clusters identify high concentrations of points in the phase subspace spanned by the daily 850-hPa winds. The *k*-means method iteratively partitions the ensemble of 15 341 days (from 1 January 1979 to 31 December 2020) without any preprocessing into *k*-clusters to minimize the sum of variances within clusters (Diday and Simon 1976). Each day is identified by the horizontal 850-hPa winds over the 10°N–30°S, 90°–30°W region. The first step of the *k*-means method is the random selection of *k* days from the 15 341 days (independent of the date of the year), which are initially considered as the cluster center. Using Euclidean distances, each daily 850-hPa wind map is assigned to the nearest center. The centroid of each of the *k* clusters is then taken as the cluster center in the second step, and the same procedure is repeated until the sum of intracluster variance stops decreasing, within a given tolerance considering a maximum of 100 iterations.

The number of *k*-clusters is evaluated by applying the Calinski–Harabasz index (Calinski and Harabasz 1974), which is based on the ratio of the sum of between-clusters dispersion and of intercluster dispersion for all clusters. This index varies from 0 (worst classification) to $+\infty$ (best classification).

Once the CPs are defined, composite analysis of different variables (e.g., rainfall and OLR) is carried out over the days assigned to each CP. These composites allow us to investigate the relationships between each CP and large-scale convection or local-scale daily rainfall.

As documented in previous studies that analyze CPs in tropical South America (Espinoza et al. 2012; da Anunciação et al. 2014; Paccini et al. 2018), the 850-hPa winds are highly relevant to describe the atmospheric circulation since they allow a proper description of the variability of the trade winds, the SALLJ, cold surges, SACZ variability, etc. (e.g., Vera et al. 2006; Espinoza et al. 2013; Carvalho et al. 2004; Mayta et al. 2018). Previous studies have shown that adding other variables (such as temperature or geopotential height at other levels of the atmosphere) in the clustering algorithm gives similar CPs and does not change the overall quality of rainfall discrimination in the Amazon (Espinoza et al. 2012).

Last, we assess the significance of the probability for the transitions between CPs by randomly reproducing (1000 times) a vector that associates each day to a specific CP, but preserving the number of days for each CP. After this resampling process, we take the 99th percentile of the randomly estimated transition probabilities. This method can be understood as a bootstrap technique (see Wilks 2006).

f. The onset of the South American monsoon system

In this study, the South American monsoon system (SAMS) onset is estimated using OLR (NOAA and CERES) and rainfall based on pentad averages. Both indices are computed on each grid point over the region extended from 5° to 25°S in STSA to provide regional specifications related to the SAMS onset. For the precipitation-based index, the SAMS onset is defined as the pentad before which the rainfall rate is less than the climatological annual rainfall (1981–2020) during 6 of 8 preceding pentads and after which the rainfall rate was greater than the climatological annual rainfall during 6 of 8 subsequent pentads. As suggested in previous studies, in the years when these thresholds did not allow identifying the SAMS onset, the duration threshold was relaxed from 6 to 5 consecutive pentads (e.g., Arias et al. 2015). For the OLR-based index, the SAMS onset is determined from the pentad after which OLR values are less than 240 W m^{-2} in 8 of 12 consecutive pentads and before which this value is exceeded in the same number of pentads (Kousky 1988; Correa et al. 2021). In this study, we prioritize the OLR-based index to analyze an independent dataset from rainfall and reanalysis-based methods (e.g., da Silva and de Carvalho 2007; Fu et al. 2013; Correa et al. 2021).

g. Trend analysis and detrended correlation

We used the Kendall test with a significance level $p < 0.05$ to evaluate temporal trends in precipitation, annual frequency of CPs, and the date of the SAMS onset. The slope of the trend is calculated using a linear regression. For the CHIRPS precipitation dataset, we analyze the 1981–2020 period; the 1979–2020 period is considered for the atmospheric variables.

The relationships between the frequency of CPs, climatic variables, and active fire account are investigated using correlation analysis on the previously detrended time series. For this purpose, we use the rank-based Kendall coefficient τ and the parametric Pearson coefficient r using a confidence level of at least 95% (significance level $p < 0.05$). The Pearson coefficient is applied as a metric of the total variance of climatic variables and active fire account explained by the frequency of CPs.

3. Results and discussion

a. Definition of the number of clusters

After applying the Calinski–Harabasz index for the 850-hPa wind data over the 10°N–30°S, 90°–30°W region for the 15 341 days, the result shows no optimum number of clusters because the index decreases while the number of clusters increases. In this study, the number of clusters were tested from 2 to 12 clusters. However, diminution in the index becomes very low after 9 clusters (not shown). In addition, according to previous studies that have already defined nine intraseasonal CPs in tropical South America (Espinoza et al. 2012; da Anunciação et al. 2014; Paccini et al. 2018) and considering the mean seasonal cycle of CPs (section 3b), we decided to retain nine groups (Fig. 1a). Then, the mean 850-hPa wind patterns of the days corresponding to each group represent our nine CPs.

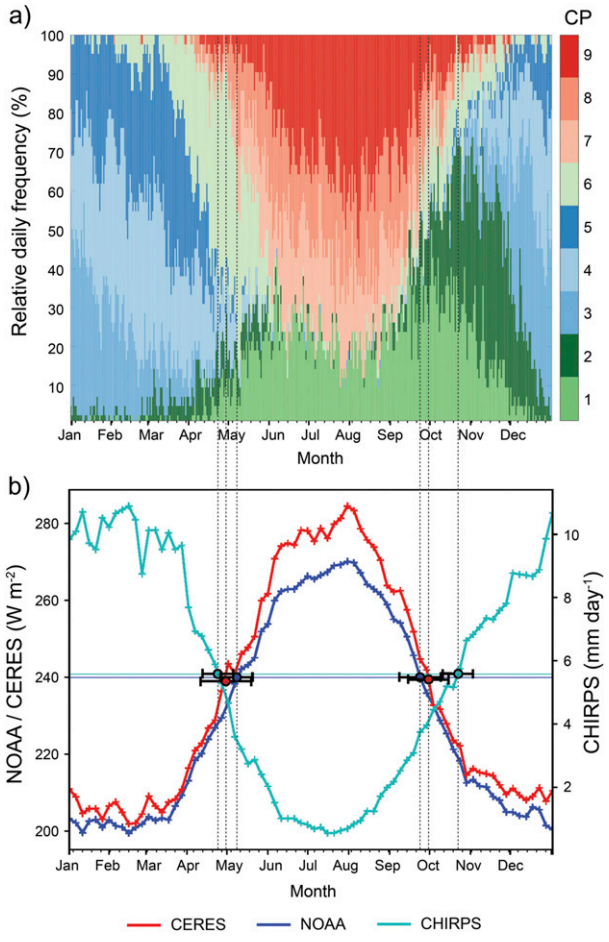

FIG. 1. (a) Relative mean daily frequency of the nine circulation patterns (CPs) defined from the *k*-means clustering of zonal and meridional daily 850-hPa winds (10°N–30°S; 30°–90°W). The *x* axis displays 365 days from 1 Jan to 31 Dec in the 42 years from 1979 to 2020. (b) Mean annual cycle of precipitation (1981–2020; green line), OLR-NOAA (1979–2020; blue line), and OLR-CERES (2001–20; red line) within the region bounded by 5°–15°S, 70°–50°W. Green, blue, and red dots show the climatological mean dates of the SAMS onset and demise estimates from precipitation, OLR-NOAA, and OLR-CERES indices, respectively. Standard deviation of the SAMS onset is also indicated for each index. The corresponding dry-season lengths are indicated with vertical dotted lines in (a) and (b).

These CPs can be interpreted as an average of each dominant meteorological state over tropical South America. As a result, each day within the period 1979–2020 was assigned to a particular CP.

b. *Mean seasonal cycle of CPs and main atmospheric features*

The mean seasonal cycle of the relative frequency of the nine CPs is shown in Fig. 1a. This seasonal distribution of CPs suggests that they can be interpreted primarily as snapshots of the mean annual cycle of the low-level wind circulation. As described in the introduction, previous studies have defined the SAMS onset and demise using pentads of precipitation or OLR over a part of southern Amazonia (50°–70°W, 15°–5°S). Following this approach, Fig. 1b shows the mean date of the SAMS onset and demise. The SAMS onset occurs around late September (pentad 54 on average with ±2.5 pentads of standard deviation) and late October (pentad 58 ± 2), according to the OLR and precipitation indices, respectively. This date also corresponds to the dry-season end (DSE) in STSA. On the other hand, the SAMS demise is usually observed between late April and early May, according to the precipitation and OLR indices, respectively (e.g., Vera et al. 2006). In addition, both OLR-NOAA and OLR-CERES data show similar dates for the SAMS onset (Fig. 1b). For interannual variability for the common period (2000–20), the SAMS onset dates estimated with both datasets are significantly correlated ($r = 0.51$; $p < 0.05$) and a higher standard deviation is observed in OLR-NOAA values (Fig. S1 in the online supplemental material).

The period corresponding to the SAMS onset is characterized by a high frequency of CP1 and CP2 (40%–70% of the time). During the austral summer (December–February), CP3, CP4, and CP5 are frequently observed (around 90% of the time). CP3 is mainly observed in December–January, whereas CP4 and CP5 are predominant in February and even in March (Fig. 1a). An abrupt diminution of the CP4 and CP5 frequencies is observed by late March and early April, while a high frequency of CP6 (40%–50% of the time) is observed. Indeed, during the SAMS demise (April–May), CP6 is observed around 60% of the time. Finally, during the austral winter (June–August corresponding to the dry season in STSA), CP7, CP8, and particularly CP9 are the most frequent (60%–80% of the time), whereas CP1 is observed during the whole dry season (10%–20% of the time) but with more frequency during the beginning of the austral winter and during the dry-to-wet transition season (Fig. 1a). In summary, the mean seasonal cycle of the frequency of CPs describes three "summer" CPs (CP3, CP4, and CP5), three "winter" CPs (CP7, CP8, and CP9), and three "transitional" CPs (CP1, CP2, and CP6) (Fig. 1a). According to Fig. 1b, CP1 and CP2 are mostly frequent during the dry-to-wet transition period in STSA (corresponding to the SAMS onset) and CP6 is most frequent during the wet-to-dry transition period (corresponding to the SAMS demise).

Table 1 indicates significant transitions within the winter CPs on one hand, and within the transitional CPs on the other hand. However, no significant transitions are detected within the summer CPs, which are the most self-persistent CPs (around 70%) and the longest spell (Table 1). The self-persistence of the winter and transitional CPs vary from 50% (CP8) to 62% (CP9). For mean length of the CPs, high values are observed for summer CPs (more than 3 days in average). These CPs also show high spells lasting at least 5 and 7 consecutive days (23%–25% of days; Table 1).

The signal of the annual cycle of the atmospheric circulation is also visible in the atmospheric composite CPs. So-called winter CPs are characterized by cross-equatorial southerly low-level winds regime and upward motion from 925 to 300 hPa in the Northern Hemisphere of South America

TABLE 1. Probability of transition (%) between the CP (rows) and another CP (column) (columns 2–10), the mean length of each CP (days) (column 11), and the percentage of days included in spells lasting at least 3, 5, and 7 consecutive days (columns 12–14). Boldface values indicate transition occurring more frequently than chance at the one-sided 99% level. To evaluate this significance, the vector that associates each day to a particular CP has been reproduced randomly 1000 times (preserving the number of days for each CP).

	CP1	CP2	CP3	CP4	CP5	CP6	CP7	CP8	CP9	Mean length	Days (in spell > 3 days)	Days (in spell > 5 days)	Days (in spell > 7 days)
CP1	**56**	7	1	4	0	11	9	4	**20**	2.3	40	21	9
CP2	**14**	**52**	10	4	4	4	1	3	0	2.1	35	20	8
CP3	3	8	**68**	9	10	0	0	0	0	3.1	41	31	25
CP4	3	6	11	**69**	10	10	1	0	1	3.2	39	29	23
CP5	0	6	10	6	**71**	5	0	0	0	3.4	40	34	24
CP6	2	**13**	0	5	5	**57**	5	**14**	1	2.3	35	24	17
CP7	3	2	0	1	0	4	**56**	**18**	7	2.3	43	19	10
CP8	**15**	6	0	1	0	3	3	**50**	**10**	2.0	38	14	4
CP9	4	0	0	1	0	6	**26**	10	**62**	2.6	41	24	18

(Figs. 2 and 3). In the extratropics (20°–40°S), an atmospheric subsidence anomaly is observed, particularly during CP7 and CP8. Atmospheric divergence at the surface predominates over southern Amazonia in CP7 and CP9. During these two CPs, southerly wind anomalies are observed from the Bolivian Amazon toward southeastern South America (SESA), particularly during CP9, which is probably related to occurrence of the SALLJ during the wintertime (e.g., Marengo et al. 2004). On the contrary, CP8 is characterized by low-level southerly wind anomalies over the entire tropical South America, to the east of the Andes (Figs. 2 and 3), which is typically observed during cold-surge intrusions in the tropical region, frequently observed during this season (e.g., Garreaud 2000; Lupo et al. 2001; Li and Fu 2006; Espinoza et al. 2013). According to the annual cycle of precipitation, the winter CPs are characterized by negative rainfall anomalies relative to mean annual values (Fig. 2), particularly over central and southern Amazon and the continental SACZ region (hereinafter the SACZ region). On the contrary, positive rainfall anomalies are observed in the extreme north of the continent, including the northwestern Amazonia in the CP8, which is related to ascending motion observed over this region (Fig. 3). At the upper levels, winter CPs are characterized by the presence of the subtropical upper-level westerlies south of 10°S (Fig. S2 in the online supplemental information).

During the dry-to-wet transitional CPs, CP1 is characterized by northerly low-level wind anomalies from the central Amazon to SESA, including SALLJ events. Negative (positive) rainfall anomalies are observed over the eastern Amazon and the SACZ regions (SESA region). Around 20°–30°S, ascending motion is observed from 850 to 200 hPa, which is associated with positive rainfall anomalies over this region (Figs. 2 and 3). On the contrary, CP2 is characterized by a northerly cross-equatorial wind regime and an extratropical southerly low-level wind intrusion toward southern and central Amazon. Consequently, during CP2, low-level winds convergence, ascending motion and positive rainfall anomalies are observed in a northwest–southeast band from central Amazonia to the northern coastal SACZ region. These atmospheric features are characteristics of the cold-air incursions from the extratropics that may trigger rainfall over central Amazon, which in combination with a northerly cross-equatorial wind regime is an important contributor of the SAMS onset (Wang and Fu 2002; Fu et al. 2013; Yin et al. 2014). Accordingly, CP2 mostly occurs during the September–November period (Fig. 1a), when the SAMS onset is usually observed (Fig. 1b). In addition, following the dry-to-wet transition period in the mean seasonal cycles of CPs, CP2 is the first CP characterized by a northerly cross-equatorial wind regime, ascending motion and positive rainfall anomalies over STSA (Figs. 2 and 3).

The so-called summer CPs (CP3, CP4, and CP5) are all characterized by a northerly cross-equatorial wind regime and intense ascending motion over the Southern Hemisphere of tropical South America (Figs. 2 and 3), which are typical characteristics of the mature phase of the SAMS (e.g., Wang and Fu 2002; Vera et al. 2006; Arias et al. 2015). At upper levels, these CPs are characterized by easterly winds at 200 hPa over the tropical Andes (Fig. S2 in the online supplemental information), which are related to positive rainfall anomalies over this region (Garreaud et al. 2003; Segura et al. 2019; Espinoza et al. 2020). Indeed, the formation of the Bolivian high at 200 hPa, which is particularly intense during CP5, characterizes the summer CPs (Fig. S2). CP4 is characterized by northerly low-level wind anomalies from the Amazon to SESA, and ascending motion is observed over the central Amazon and SESA. Positive rainfall anomalies are observed over these regions. On the contrary, during CP3 and CP5, low-level southerly wind intrusions are observed in the southernmost Amazonia (Fig. 2). Related to this feature, low-level wind convergence, ascending motion and positive rainfall anomalies are intense over the southeastern Amazon, the tropical Andes, and the SACZ regions (Figs. 2 and 3). The above-described summer CPs depict the main intraseasonal patterns characterizing this season, such as the SESA–SACZ dipole (CP4–CP3), the intraseasonal variability of the SACZ (CP3–CP5), and the intensity of the Bolivian high (CP5) (e.g., Silva Diaz et al. 1983; Nogués-Paegle and Mo 1997; Carvalho et al. 2004).

During the transitional wet-to-dry CP6, southerly winds anomalies predominate at lower levels, including a southerly cross-equatorial wind regime (Fig. 2). Low-level wind

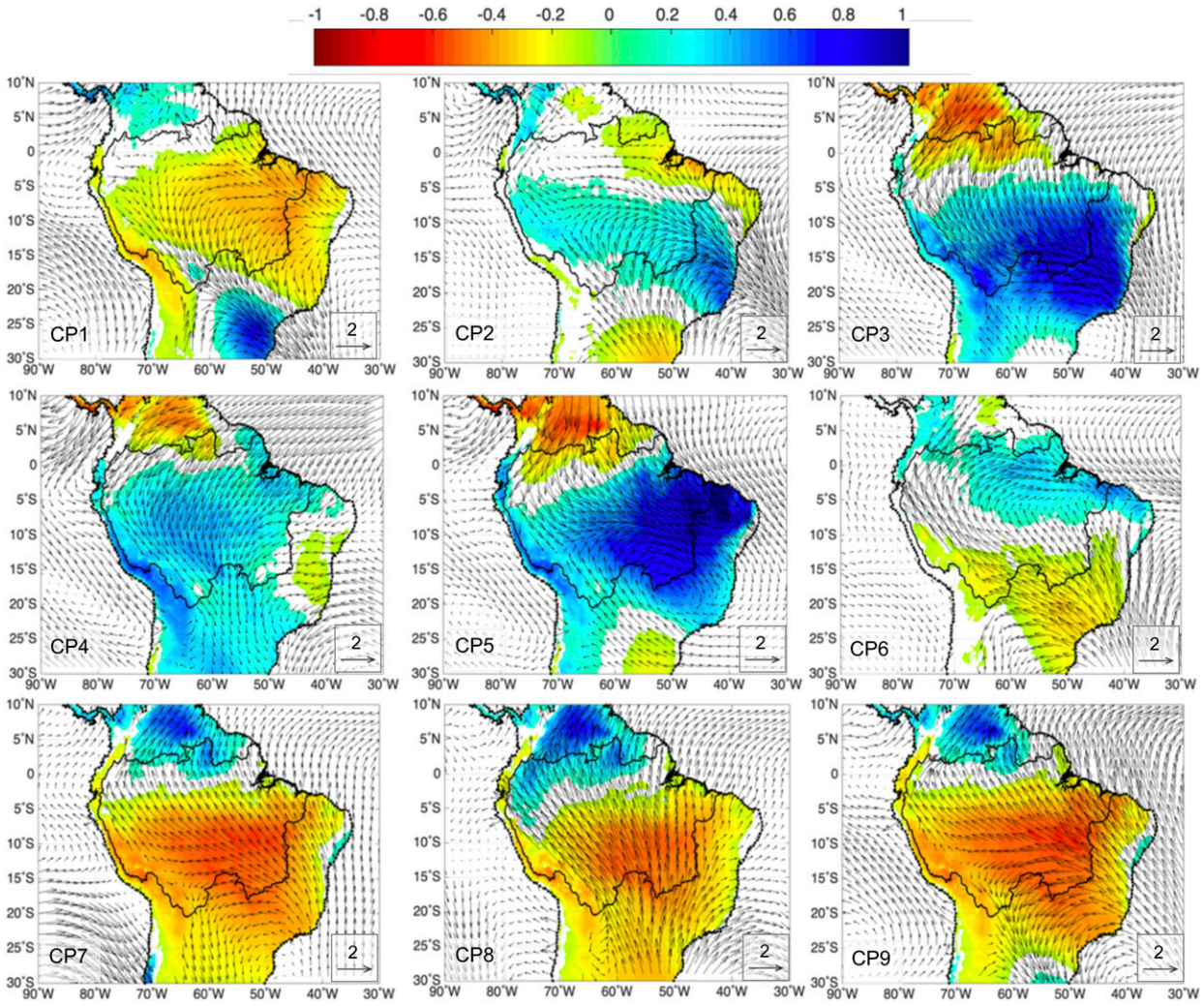

FIG. 2. Mean 850-hPa winds (vectors) and precipitation (shadings) standardized anomalies for the nine CPs defined using *k*-means clustering of the standardized anomalies of 850-hPa winds for the period 1979–2020. Only standardized precipitation anomalies higher than 0.1 or lower than −0.1 are plotted. The black outline indicates the boundary of the Amazonian region.

divergence is observed in STSA and ascending motion predominates over the equatorial region from 925 to 300 hPa (Fig. 3). At upper levels, subtropical westerlies are observed south of 15°S (supplemental Fig. S2). In relation to these features, negative (positive) rainfall anomalies are observed over the SACZ region and southern Amazon (northeastern Amazon). Note that the rainfall annual peak in the northeastern Amazon is observed during April–May (Espinoza et al. 2009), which is in accordance with a major frequency of CP6 during these months (Fig. 1).

c. *Changes in the frequency of CPs and the SAMS onset*

In this section, we investigate potential changes in the frequency of CPs during the 1979–2020 period. According to Fig. 1b, precipitation in southern Amazonia begins to increase from mid-July, and the July–October period corresponds to the increasing portion of the seasonal cycle of precipitation that precedes the wet season. In this study, we define the July–October period as the extended dry-to-wet transition season in STSA, which corresponds to a portion of the extended dry season defined by Zemp et al. (2017). Table 2 shows that this season is characterized by significant trends in the frequency of two CPs in the period 1979–2020. While a decreasing trend is observed in the frequency of CP2 during September–October (corresponding to the mean date of SAMS onset), the frequency of CP9 significantly increases during July–September. No trends are detected in other CPs during the July–October period (Table 2). During December–January, a significant increase in the frequency of CP4 is also observed; however, because the objective of this study is to investigate changes in atmospheric circulation during the dry-to-wet transition period in STSA, the following analysis will concentrate on the variations of CP2 and CP9, which are the only CPs showing significant trends during this season (according to Table 2), and associated rainfall anomalies during the July–October season.

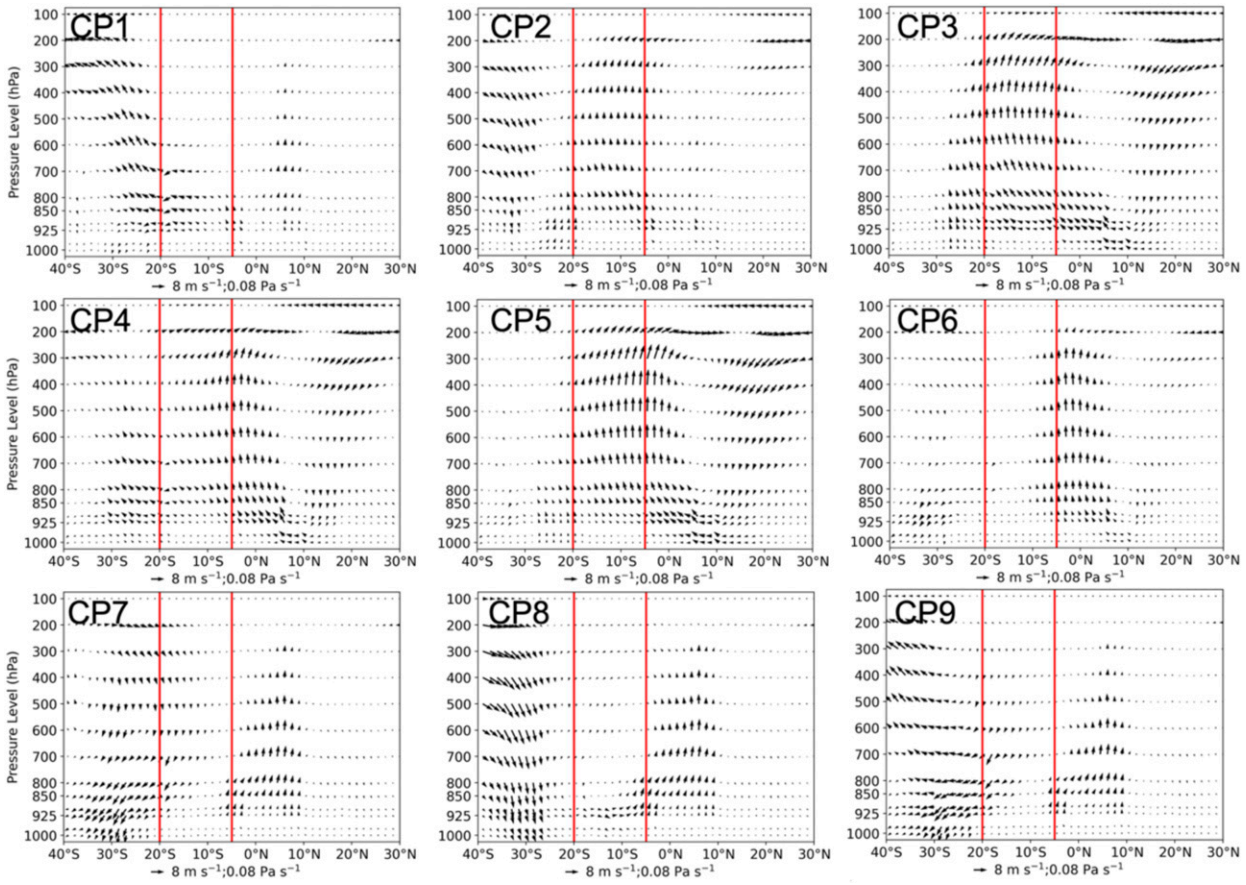

FIG. 3. Meridional and vertical wind anomalies (vectors) zonally averaged over the 70°–40°W region for the nine CPs defined in Fig. 1a. Vertical red lines indicate the boundaries of the southern Amazon (from 5° to 20°S).

Considering the entire July–October season, Fig. 4a shows a significant increase and decrease of the CP9 and CP2 frequency, respectively, at $p < 0.01$. During the decade of the 1980s, CP9 was observed around 20% of the time and this frequency increased to 35% for the 2010–20 period. Higher frequencies of CP9 were observed in 2017, 2012, 2007, 2020, and 2014. In contrast, the frequency of CP2 changed from 13% of the time during the 1980s to 7% in the last decade. For example, CP2 was rarely observed in 2017, 2015, and 2012. In summary, during the dry-to-wet transition season in STSA, the winter CP9 is most frequently observed during the last years, in contrast to the transitional CP2, which become rarely observed. Because CP2 is related to atmospheric mechanisms associated with the SAMS onset (section 3b), these results suggest that the delayed onsets of the SAMS documented in the literature may be linked to a decrease and increase of CP2 and CP9, respectively, during the dry-to-wet transition season.

Figure 4b reveals that the higher occurrence of CP9 and lower occurrence of CP2 during the July–October season are associated with an anomalous intensification of the southerly cross-equatorial wind regime, with easterly low-level winds in southeastern Amazonia and the subtropical branch of the SALLJ. In general, Fig. 4b also shows that the low-level winds from the tropical North Atlantic toward the continent are weakened. Consequently, wind divergence and negative rainfall anomalies are observed over most of STSA. Frequencies of CP2 and CP9 are not significantly correlated considering a detrended analysis for the 1979–2020 period. In accordance with these atmospheric mechanisms, Fig. 4c shows that the higher occurrence of CP9 and lower occurrence of CP2 during the July–October season are associated with a diminution of the deep convective clouds over southern Amazonia and SACZ regions, while an increase of deep convective clouds is observed over northern South America and the SESA region.

As described in the introduction, studies based on precipitation and OLR indices have identified a trend of late onsets of the SAMS since 1979 in association with a longer dry season in the southern Amazon. Based on the OLR index and for the 1979–2020 period, Fig. 5a shows that a trend toward late wet-season onsets is observed in southeastern Amazonia, southern Amazonia (mainly Bolivian Amazon), and western Amazonia. Consistently, these regions are characterized by a significant decrease of rainfall and increase of dry-day frequency (DDF), defined as days with precipitation <1 mm day^{-1}) during the dry-to-wet transition season (Figs. 5b,c). However, some discrepancies between the trend of the wet-season onset date and rainfall are observed in western Amazonia, where positive and negative trends are observed; due to the differences in the

TABLE 2. The τ coefficient resulting from the Kendall trend test on the frequency of CPs during the period 1979–2020. Boldface numbers indicate statistical significance at $p < 0.05$.

CP	Jan	Feb	Mar	Apr	May	Jun	Jul	Aug	Sep	Oct	Nov	Dec
1	—	—	—	—	—	—	—	—	—	—	—	—
2	—	—	—	—	—	—	—	—	**−0.25**	**−0.24**	—	—
3	—	—	—	—	—	—	—	—	—	—	—	—
4	**0.24**	—	—	—	—	—	—	—	—	—	—	**0.28**
5	—	—	—	—	—	—	—	—	—	—	—	—
6	—	—	—	—	—	—	—	—	—	—	—	—
7	—	—	—	—	—	—	—	—	—	—	—	—
8	—	—	—	—	—	—	—	—	—	—	—	—
9	—	—	—	—	—	—	**0.26**	**0.26**	**0.26**	—	—	—

spatial resolution of the datasets, as well as the complex seasonal cycles of precipitation over this region (Espinoza et al. 2009), comparison becomes difficult. Nonetheless, according to previous studies, Fig. 5 confirms that drier conditions during the dry-to-wet transition season and a more frequent occurrence of delayed SAMS onsets have characterized the southeastern Amazonia during the last four decades.

To analyze the relationship between the frequency of CPs and rainfall during the dry-to-wet transition period in STSA, a detrended correlation analysis is carried out between the frequency of CPs and rainfall (for the 1981–2020 period) and the SAMS onset index (for the 1979–2020 period). During the years characterized by anomalously more CP9 than usual, negative rainfall anomalies and positive DDF anomalies predominate over the southeastern Amazonia and the SACZ region (Figs. 6a,c). The opposite rainfall signal is observed during the years characterized by anomalously more CP2 than usual, with rainfall anomalies centered over the extreme eastern Amazonia and eastern Brazil (Figs. 6b,d). The same analysis considering the other seven CPs shows no significant correlations with rainfall or OLR-based SAMS onset for the July–October period (not shown). In accordance with these results, Fig. 6e shows that late

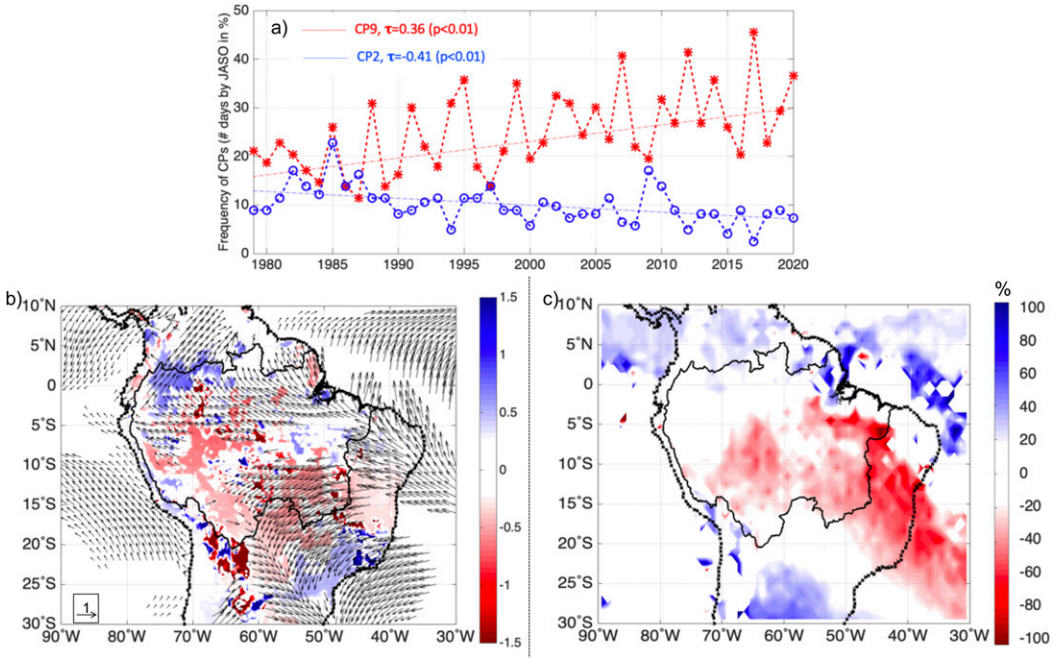

FIG. 4. (a) The 1979–2020 evolution of the frequency of days with CP9 (red line) and CP2 (blue line) for the July–October (JASO) season. The frequency of CPs (number of days by season) is indicated in percentage of the total number of JASO days. The τ coefficients and trends according to Kendall test are given. (b) Difference of 850-hPa winds (vectors) and precipitation (shading) standardized anomalies between CP9 minus CP2 during JASO. Only standardized differences of precipitation and winds anomalies higher than 0.2 or lower than −0.2 are plotted. The black outline indicates the boundary of the Amazonian region. (c) Difference of the number of days with deep convective clouds between CP9 minus CP2 expressed as a percentage of the total JASO days characterized by deep convective clouds (2000–20). Only percentage differences higher than 20% or lower than −20% are plotted.

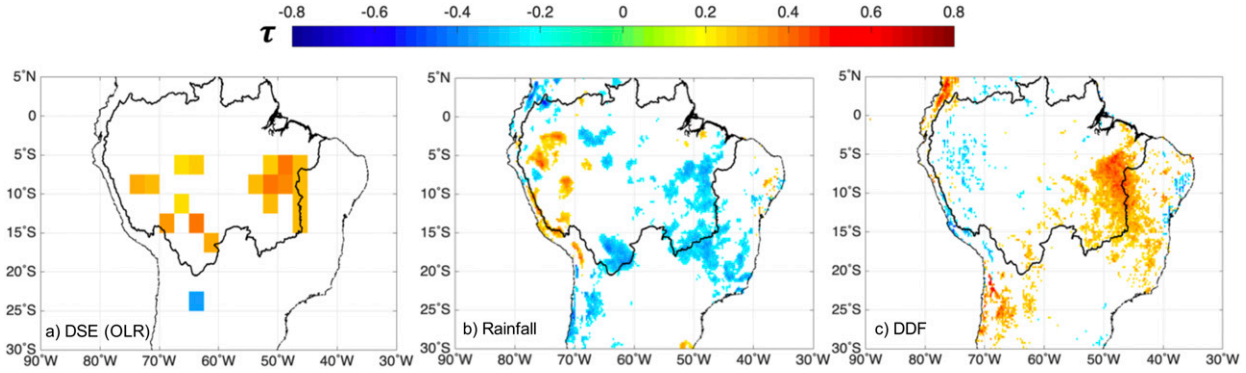

FIG. 5. Spatial distribution of Kendall coefficient values τ ($p < 0.05$) indicating the trend for (a) 1979–2020 date of the wet-season onset [or dry-season end (DSE)], (b) 1981–2020 July–October rainfall, and (c) 1981–2020 July–October dry-day frequency (DDF). Only values with $p < 0.05$ are displayed.

wet-season onset over eastern Amazonia is significantly associated with a higher frequency of CP9. In contrast, the variability of the frequency of CP2 shows a limited influence in the date of the SAMS onset (Fig. 6f). Based on running 31-day window correlation analysis, Fig. 7 shows that the frequency of CP9 and CP2 is positively and negatively correlated, respectively, with the date of the wet-season onset computed over the 5°–15°S, 47.5°–60°W region (black box in Fig. 6e). These correlations are particularly significant (even after removal of the long-term trend) considering CP9 and when the running correlation is centered from mid-August to mid-September, thus around one month before the occurrence of the regional-scale onset. However, correlations suddenly decay around two weeks before the wet-season onset (Fig. 7). This figure suggests, for example, that an anomalously high frequency of CP9 around mid-to-late August (i.e., when the running correlations between SAMS onset date and CP9 frequency peak) is linearly related to a delayed SAMS onset (and vice versa for an anomalously low frequency of CP9 associated with an earlier SAMS onset than usual). These results indicate that the frequency of CP9 and CP2 during the dry-to-wet transition period modulates the rainfall variability over southeastern Amazonia and the SACZ region, including the SAMS onset (Figs. 6 and 7). The latter is particularly associated with the frequency of CP9.

According to previous studies, a delayed SAMS onset is associated with a blocking of cold-air incursions from the extratropics during the dry-to-wet transition period that would trigger rainfall over STSA (Li and Fu 2006). Our results are in accordance with these mechanisms, considering that the frequency of CP2 (characterized by cold-air incursions in STSA; Fig. 2) is lower during the last years in opposition to the frequency of CP9, which is characterized by southerly wind anomalies from the Amazon basin to the SESA region (Fig. 2). In addition, the frequency of CP9 (CP2) is positively (negatively) correlated with CIN anomalies over southeastern Amazonia and the SACZ region during the July–October season (Figs. S3a,b in the online supplemental information), indicating that CP9 is related to a larger convective inhibition. Considering a shorter period (2000–20), our analysis also shows that the lower frequency of CP2 and higher frequency of CP9 are associated with a diminution of deep convective clouds over the SACZ region and parts of the southern Amazonia (Fig. 4c; see also supplemental Figs. S3c,d). Previous studies also indicate that a poleward displacement of the subtropical jet over South America is a relevant mechanism contributing to a delayed SAMS onset (Li and Fu 2004; Yin et al. 2014). However, for differences between CP9 and CP2, no significant changes were observed in the position and intensity of the subtropical jet during the July–October season (not shown). Therefore, further analyses are necessary to describe intraseasonal changes of the subtropical jet over South America.

More recent studies also suggest that drier conditions in southern Amazonia are related to a reduction of deep convection and increasing atmospheric subsidence over this region during the dry-to-wet transition season (e.g., Arias et al. 2015; Agudelo et al. 2019; Espinoza et al. 2019a). Enhanced Walker and Hadley circulations (modulated by warm conditions in the Atlantic and the variability of Pacific SSTs) have intensified this atmospheric subsidence over the southern Amazon during the last decades (Yoon and Zeng 2010; Arias et al. 2015; Espinoza et al. 2016; Haghtalab et al. 2020). Nevertheless, the frequency of CPs during the July–October season is not significantly correlated with SST considering a detrended analysis of the time series (not shown). In agreement with previous studies, CP2, characterized by intense ascending motion and deep convective clouds over the southern Amazon and the SACZ region, has become less frequent during recent years in contrast to CP9, characterized by atmospheric subsidence over STSA (Figs. 3 and 4c). Therefore, these results suggest that the frequency of CP9 (which is typically a winter CP) during the dry-to-wet transition period is a good indicator of the duration of the dry season in southeastern Amazonia and the SACZ region.

d. Atmospheric circulation patterns and the intensity of the fire season (1999–2020)

The dry-season period (especially its end) in STSA is frequently associated with the fire season intensity (see the introduction and Fig. 8) as observed in many other tropical areas (e.g., van der Werf et al. 2008). According to Fig. 6, the delay of the SAMS onset is particularly significant over a region that includes the Brazilian

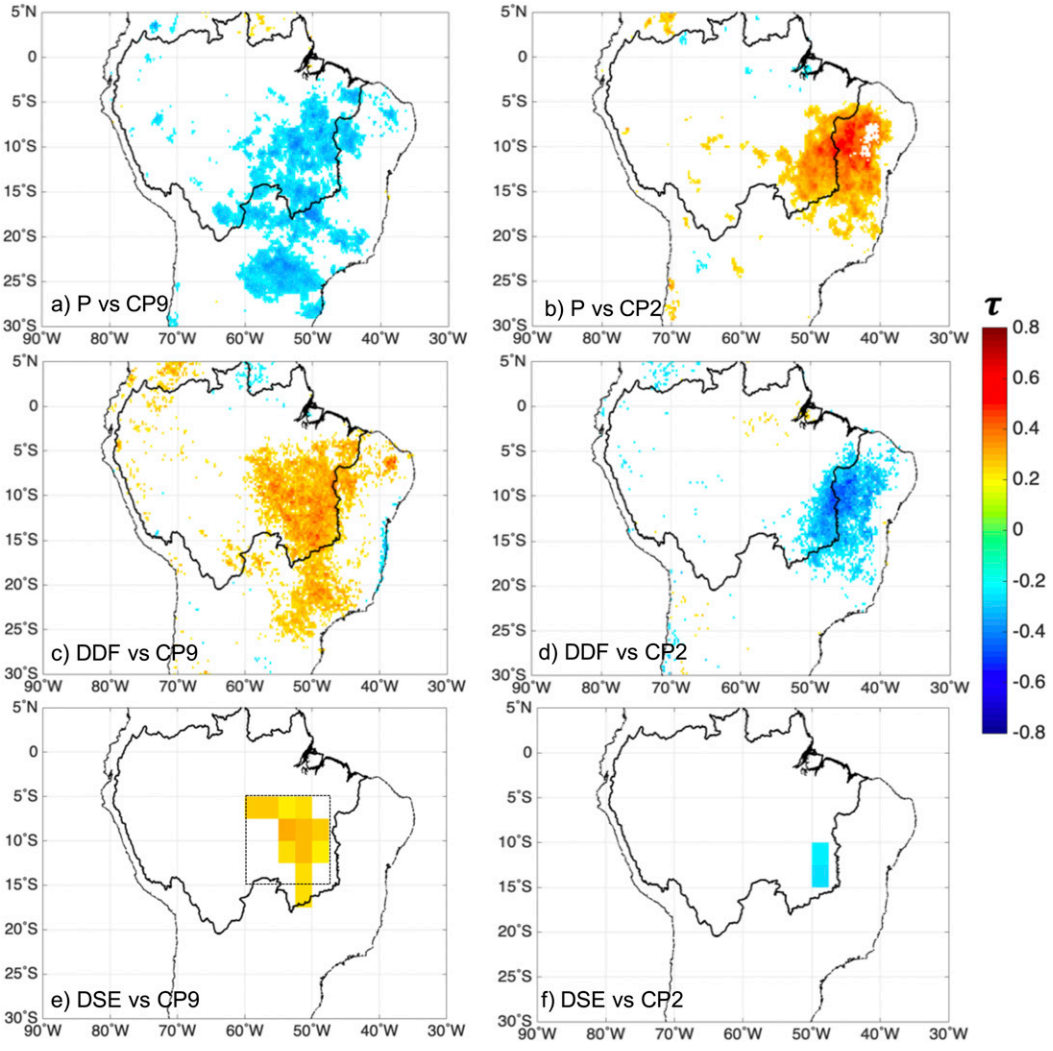

FIG. 6. Spatial distribution of τ values ($p < 0.05$) between July–October rainfall and the frequency of (a) CP9 and (b) CP2 for the period 1981–2020, July–October DDF and the frequency of (c) CP9 and (d) CP2 for the period 1981–2020, and 1979–2020 date of the wet-season onset (or DSE) and the frequency of (e) CP9 and (f) CP2. Time series were linearly detrended before applying the Kendall correlation. Only values with $p < 0.05$ are displayed. In (e), the region bounded by 5°–15°S, 60°–47.5°W is indicated with a dotted black rectangle. Over this region, the running correlations between the wet-season onset and frequencies of CP9 and CP2 are computed in Fig. 7, below.

states of Maranhão, Tocantins, and Goiás (Fig. 8a). Figure 9a shows the scatterplot between the date of SAMS onset (or the DSE computed from OLR-NOAA) over the 5°–15°S, 47.5°–60°W region (black box in Fig. 6e) and active fire counts anomalies averaged over these Brazilian states for the July–October season. Both variables are significantly correlated ($r = 0.51$ and $\tau = 0.39$, with $p < 0.05$), confirming that years with a delayed SAMS onset are frequently characterized by an intense active fire season, for instance in 2007, 2010, and 2012. However, in some years (e.g., 2020), the late SAMS onset is not associated with high active fire anomalies. This correlation suggests that the date of the SAMS onset explains around 25% of the total variance of active fire counts in July–October. No significant correlations are found when fire activities are analyzed in other Brazilian states. In the next part of this section, we investigate if the frequency of CPs can be related to the intensity of the fire season in STSA.

Considering the July–October season, correlation between active fire counts and the frequency of CPs are not significant at $p < 0.01$, with the exception of CP9. For this reason, in this section we analyze the relationship between the CP9 frequency (which is particularly relevant for determining the dry-season length in this region and its more or less delayed transition to the next wet season) with the fire activity during July–October season. As shown in Figs. 6a and 6c, the frequency of both CP9 and dry days during the July–October season are significantly correlated over the southeastern Amazon, the Cerrado region, and the SACZ region, involving the Brazilian states of Maranhão, Tocantins, Goiás, São Paulo, and parts of Mato Grosso and Pará. Given the active fire counts data availability (see section 2), we

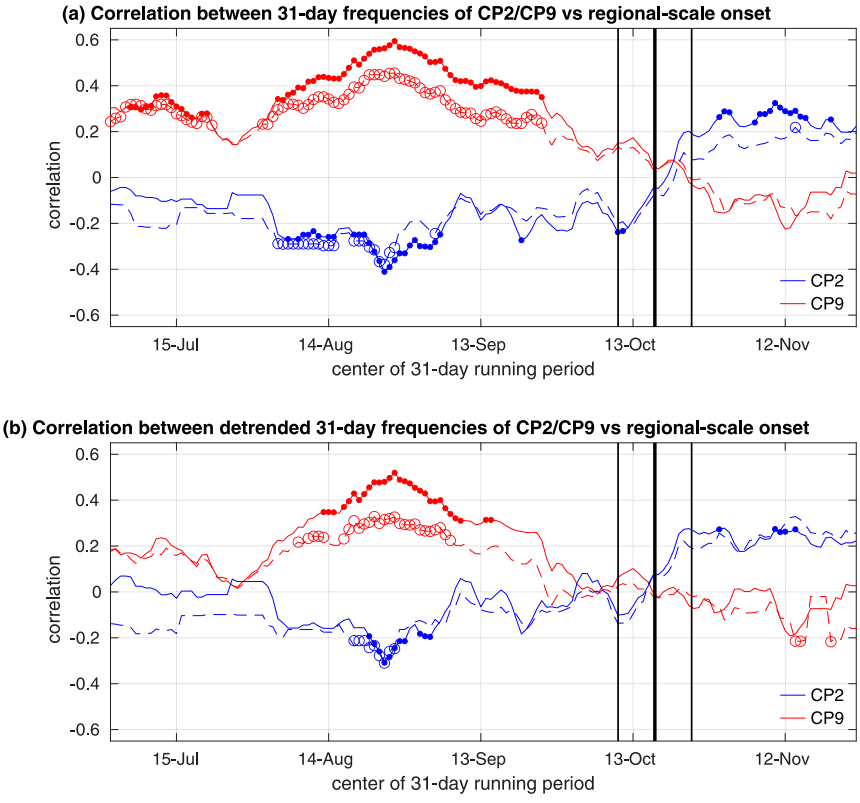

FIG. 7. Pearson (solid line with dots) and Kendall (dashed line with circles) running correlations between frequency of CP2 (in blue) and CP9 (in red) and SAMS onset date (defined over 5°–15°S, 60°–47.5°W, the area shown as a black box in Fig. 6e). The correlations between the frequency of either CP9 or CP2 on one hand and SAMS onset date on the other hand are computed on running 31-day windows centered on days indicated on the *x* axis. Dots and open circles respectively indicate significant Pearson and Kendall correlations at $p < 0.05$ according to a random-phase test using 1000 simulations. Shown are (a) the raw correlations and (b) the correlations after a linear trend is removed from all time series. The vertical thick and thin black lines are the mean and ±1 std dev onset SAMS dates, respectively.

investigate the relationship between the frequency of CP9 and fire counts on the states where the influence of CP9 is more relevant for dry conditions: Maranhão, Tocantins, and Goiás in the southeastern Amazon and Cerrado region, and São Paulo in the SACZ region (Fig. 8). Note that fires in São Paulo occur mostly in farming areas and particular characteristics have been identified in protected areas and their buffer zones (e.g., Conciani et al. 2021). No significant relationships were obtained considering fire counts in Mato Grosso and Pará states (not shown), probably because these extensive states also cover regions where the influence of CP9 on dry conditions is not significant.

In Maranhão, Tocantins, and Goiás, a higher frequency of CP9 is significantly associated with an intense fire season during July–October (Fig. 9b). Over these states, the frequency of CP9 explains around 35% of the total variance of the fire counts variability during the 1999–2020 period ($r = 0.59$, $\tau = 0.46$, and $p < 0.01$). For fire counts in the state of São Paulo, higher correlation is obtained considering a shorter period from September to October, corresponding to the end of the fire seasons and the split between dry and wet seasons, where the frequency of CP9 explains 44% of the active fire counts ($r = 0.66$, $\tau = 0.60$, and $p < 0.01$) (Fig. 9c). Note that no significant trend is detected for CP9 during the shorter 1999–2020 period and correlation between frequency of CP9 and active fire counts for this common period provides similar results if a detrended analysis is applied (both correlation coefficients are indicated in Fig. 9). These results indicate that a higher frequency of CP9 during the dry-to-wet period would intensify the fire season, leading to an increase of fire counts during September–October in the state of São Paulo and during July–October for Maranhão, Tocantins, and Goiás. More interesting, our findings show that the CPs, which are based only on low-level wind circulation, provide relevant information about the atmospheric situations that can enhance the risk of stronger fire activity. For instance, in 2007, 2012, 2014, and 2017, the higher fire counts are associated with high frequency of CP9 in both regions (Figs. 9b,c). However, some discrepancies can be observed. For example, in 2007 the highest fire season was observed over the states of Maranhão, Tocantins, and Goiás

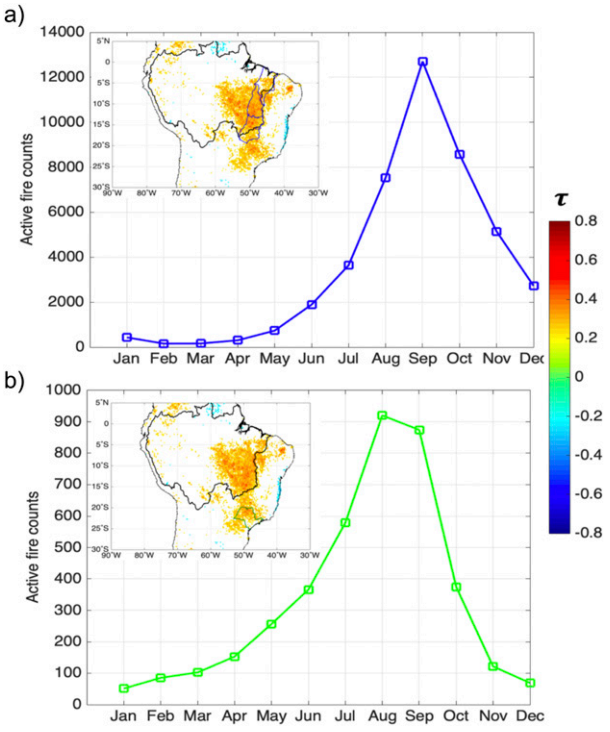

FIG. 8. Mean 1999–2020 seasonal cycle of active fire counts averaged over (a) the states of Maranhão, Tocantins, and Goiás and (b) the state of São Paulo. The inset panels show the same area as in Fig. 6c, but indicating the boundaries of the states of Maranhão, Tocantins, and Goiás (with blue lines) in (a) and São Paulo (with a green line) in (b).

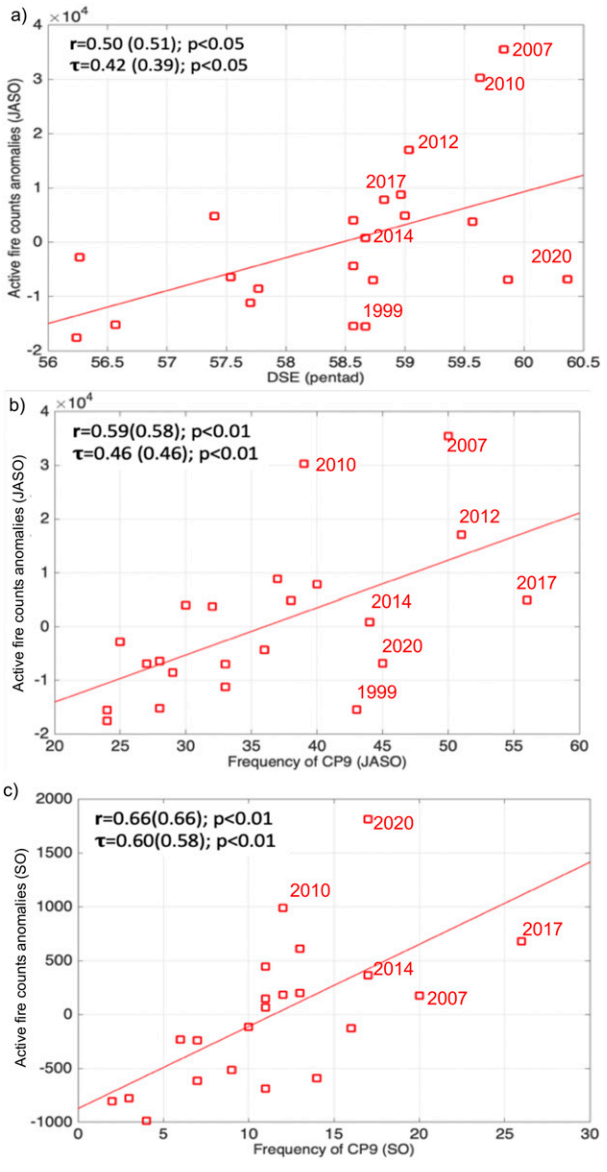

FIG. 9. (a) A 1999–2020 scatterplot between the date of DSE (in pentads computed from OLR-NOAA data) over the 5°–15°S, 47.5°–60°W region (black box in Fig. 6e) and July–October averaged active fire counts anomalies in the states of Maranhão, Tocantins, and Goiás. (b) A 1999–2020 scatterplot between the July–October frequency of CP9 and averaged active fire counts anomalies in the states of Maranhão, Tocantins, and Goiás. (c) A 1999–2020 scatterplot between the September–October frequency of CP9 and averaged active fire counts anomalies in the states of São Paulo. Active fire counts anomalies are computed using the climatological period of 1999–2000. The r and τ values resulting from Pearson and Kendall correlation, respectively, between DSE, CP9, and active fire counts anomalies are indicated. Values between parentheses correspond to correlations from detrended time series. Years with high frequency of CP9 are indicated.

and in 2020 it was observed over the state of São Paulo; however, these events are not necessarily explained by the highest frequency of CP9. On the other hand, high active fire accounts were reported during July–October 2010, but the frequency of CP9 was between the mean observed values. Indeed, fires activity during 2010 has been associated with historical drought conditions in tropical South America throughout the year, which is translated into a delayed SAMS onset (Fig. 9a). This event was mainly related to El Niño, during the austral summer, and to anomalously warm conditions in the north tropical Atlantic during the austral autumn and winter (Espinoza et al. 2011; Marengo et al. 2011). Previous studies have demonstrated that biomass burning is primarily related to human factors, such as deforestation and land management activities; however, climate factors, such as seasonal droughts (related to El Niño or warm conditions in north tropical Atlantic), also modulate fire activities (Fernandes et al. 2011; Alencar et al. 2015; Aragão et al. 2018; Cunha et al. 2019; Libonati et al. 2021; da Silva et al. 2020).

4. Conclusions and final remarks

The dry season in southern tropical South America has lengthened in recent decades, mainly associated with a delayed onset of the South American monsoon system. In this study, we

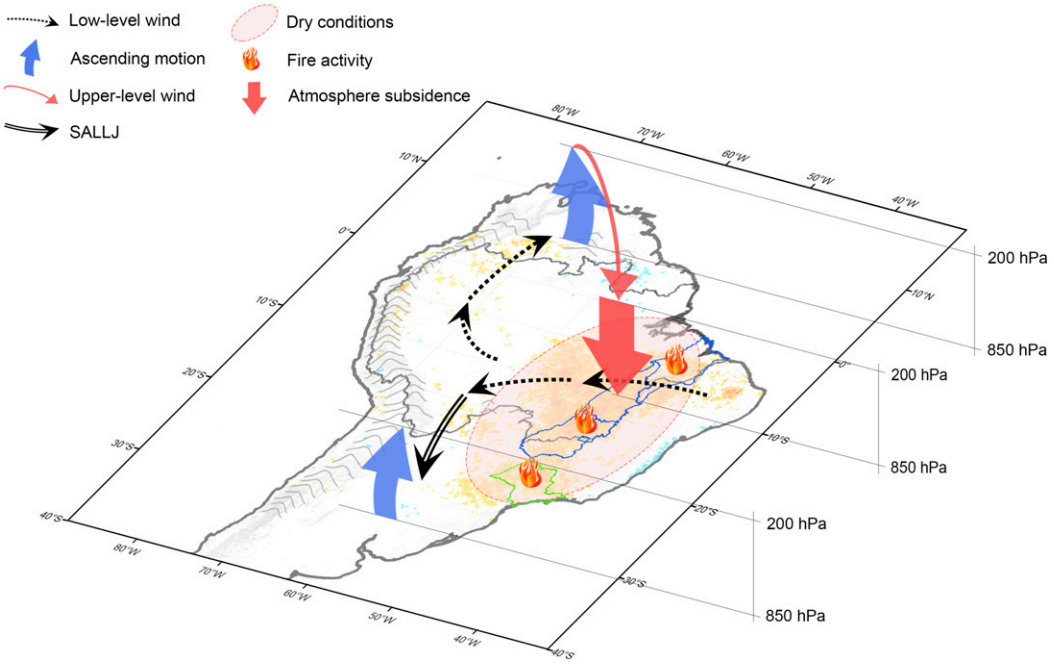

FIG. 10. Schematic representation of the main changes in atmospheric circulation related to the increasing trend of the CP9 frequency and decreasing trend of the CP2 frequency during the dry-to-wet transition season over south tropical South America (1979–2020) and associated impacts on dry conditions and fire activity. The boundaries of the states of Maranhão-Tocantins-Goiás and of São Paulo are indicated by blue and green lines, respectively.

have analyzed the characteristics of atmospheric variations over tropical South America using the pattern recognition framework of weather typing, defined here as atmospheric circulation patterns. This study aimed to (i) identify the CPs all year around, in particular during the dry-to-wet transition season over STSA, (ii) analyze the temporal evolution of the CPs observed during the dry-to-wet transition season [July–October (JASO)] during the 1979–2020 period, in relation to rainfall variability and the occurrence of delayed SAMS onsets, and (iii) analyze the impact of a lengthened dry season in STSA, defined by the CPs, on the fire activity in the region.

The definition of the CPs is based on unfiltered daily low-level wind anomalies from 1979 to 2020 within the region bounded by 10°N–30°S, 90°W 30°W. Following a *k*-means method, daily low-level winds were gathered into nine recurrent atmospheric states or CPs: three ''winter'' CPs (CP7, CP8, and CP9), three ''summer'' CPs (CP3, CP4 and CP5), and three ''transitional'' CPs (CP1, CP2, and CP6). While CP6 is particularly frequent during the wet-to-dry season in STSA, CP1 and CP2 are characteristics of the dry-to-wet transition season. After a description of the main atmospheric characteristics of each CP, we analyzed the trends in the frequency of CPs for the 1979–2020 period. Significant changes are observed during the dry-to-wet transition season over STSA (JASO). During JASO, the winter CP9 is most frequently observed (from 20% of the time in the 1980s to 35% of time in the last decade) in contrast to the transitional CP2, which become rarely observed (from 13% to 7%). The main atmospheric features related to changes in CPs' frequency during the dry-to-wet transition season in STSA are schematically summarized in Fig. 10. Considering the 1981–2020 period, our results show that drier conditions over the southeastern Amazonia and the continental part of the SACZ during the dry-to-wet transition season in STSA are related to a high frequency of CP9 and low frequency of CP2. Therefore, the above described ''replacement'' of CP2 by CP9 can be associated with atmospheric changes contributing to a delayed SAMS onset during the 1979–2020 period (Fig. 10).

Previous studies have described a blocking of cold-air incursions from the extratropics as mechanisms associated with a delayed SAMS onset (Garreaud 2000; Li and Fu 2004; Fu et al. 2013). Our results, based on a CPs partitioning, agree with these mechanisms considering that the frequency of CP2 (characterized by active cold-air incursions and deep convective clouds over STSA) decreases during the last years. In contrast, CP9 is characterized by southerly wind anomalies from the Amazon basin to the SESA region and lack of convective clouds cover (Fig. 10). In relation to a higher frequency of CP9, a reduction of deep convection, and increasing atmospheric subsidence are observed in STSA, where drier conditions are reported during the dry-to-wet transition season for the 1979–2020 period (Fig. 10). These changes in atmospheric circulation have been associated with an enhanced Hadley circulation, which intensifies atmospheric subsidence (ascendance) over STSA (northern South America) (e.g., Arias et al. 2015; Agudelo et al. 2019; Espinoza et al. 2019a). On the other hand, studies suggest that a delayed

onset of the rainy season in the southern Amazon can be influenced by anthropogenic forcing, such as deforestation (Debortoli et al. 2015; Alves et al. 2017; Leite-Filho et al. 2019; Ruiz-Vásquez et al. 2020). Thus, studies about changes in the coupling between large-scale atmospheric circulation and local land surface processes are necessary in order to reduce uncertainties in the future projections of the water cycle in tropical South America.

According to our results, a delayed SAMS onset, and a higher frequency of CP9 during the dry-to-wet period in STSA, would intensify the fire season in this region. Over the Brazilian states of Maranhão, Tocantins, and Goiás the date of the SAMS onset explains around 25% of the interannual variability of fire counts activity during the period of 1999–2020. However, considering the states of Maranhão, Tocantins, Goiás, and São Paulo the frequency of CP9 explains around 35%–44% of the fire counts activity. In 2007, 2012, 2014, and 2017, higher fire counts are associated with a higher frequency of CP9 in these regions (Fig. 10). In accordance with previous works, our results show that fire activity can be modulated by climate factors identified by mean of CPs. Nonetheless biomass burning is primarily triggered by human factors, such as deforestation and land management activities, which are highly heterogeneous into the Brazilian states analyzed in this study (Aragão et al. 2018; Conciani et al. 2021; Cunha et al. 2019; Libonati et al. 2021; da Silva et al. 2020). These results encourage further analysis to identify natural conditions preconditioning fire activities in STSA, taken under consideration meteorological (based on CPs) and hydrological conditions (e.g., soil moisture) during the dry-to-wet transition period that can modulate vegetation stress (e.g., Arias et al. 2020; Gutierrez-Cori et al. 2021).

Based on the CP approach, these results provide further insights in the identification of atmospheric states particularly relevant for understanding the dry-to-wet transition season over STSA and the SAMS onset. In addition, these CPs, which are based only on low-level wind circulation, provide new perspectives for seasonal forecasting systems of the dry-season length and related impacts on the intensity of the fire season over this region. Indeed, wind circulation is frequently better simulated by global, regional, and forecasting models in comparison with precipitation, temperature, or soil moisture, which are relevant variables for the vegetation activity. Therefore, based on atmospheric models or reanalysis data, the method described in this study can be applied as a practical operational tool to identify CPs, in near real time, and anticipate the SAMS onset based on winds circulation.

Our results highlight the need to improve our understanding about interactions among land surface processes, atmospheric convection, and biomass burning, which may modulate the SAMS onset, including changes in oceanic/continental moisture sources and recycling moisture (e.g., Wright et al. 2017; Ruiz-Vásquez et al. 2020). Further studies about this topic are particularly relevant considering the projected increase of drought conditions in STSA (Boisier et al. 2015; Cook et al. 2020; Moon and Ha 2020; Parsons 2020; Sena and Magnusdottir 2020) and the impact of deforestation in the regional water and carbon cycles (Staal et al. 2018).

Acknowledgments. This research has been supported by the French AMANECER-MOPGA project funded by ANR and IRD (ANR-18-MPGA-0008), and by the ACE-Amazon project funded by the regional program CLIMAT-AmSud (21-CLIMAT-01). Author P. A. Arias has been funded by MINCIENCIAS through Grant 80740-490-2020.

REFERENCES

Agudelo, J., P. A. Arias, S. C. Vieira, and J. A. Martínez, 2019: Influence of longer dry seasons in the southern Amazon on patterns of water vapor transport over northern South America and the Caribbean. *Climate Dyn.*, **52**, 2647–2665, https://doi.org/10.1007/s00382-018-4285-1.

Alencar, A. A., P. M. Brando, G. P. Asner, and F. E. Putz, 2015: Landscape fragmentation, severe drought, and the new Amazon forest fire regime. *Ecol. Appl.*, **25**, 1493–1505, https://doi.org/10.1890/14-1528.1.

Alves, L., J. Marengo, R. Fu, and R. Bombardi, 2017: Sensitivity of Amazon regional climate to deforestation. *Amer. J. Climate Change*, **6**, 75–98, https://doi.org/10.4236/ajcc.2017.61005.

Aragão, L. E. O., L. O. Anderson, M. G. Fonseca, T. M. Rosan, L. B. Vedovato, and F. H. Wagner, 2018: 21st century drought-related fires counteract the decline of Amazon deforestation carbon emissions. *Nat. Commun.*, **9**, 536, https://doi.org/10.1038/s41467-017-02771-y.

Arias, P. A., R. Fu, C. S. Vera, and M. Rojas, 2015: A correlated shortening of the North and South American monsoon seasons in the past few decades. *Climate Dyn.*, **45**, 3183–3203, https://doi.org/10.1007/s00382-015-2533-1.

——, J. A. Martínez, J. D. Mejía, M. J. Pazos, J. C. Espinoza, and S. Wongchuig-Correa, 2020: Changes in normalized difference vegetation index in the Orinoco and Amazon River basins: Links to tropical Atlantic surface temperatures. *J. Climate*, **33**, 8537–8559, https://doi.org/10.1175/JCLI-D-19-0696.1.

Arvor, D., B. M. Funatsu, V. Michot, and V. Dubreui, 2017: Monitoring rainfall patterns in the southern Amazon with PERSIANN-CDR data: Long-term characteristics and trends. *Remote Sens.*, **9**, 889, https://doi.org/10.3390/rs9090889.

Barichivich, J., E. Gloor, P. Peylin, R. J. W. Brienen, J. Schönegartn, J. C. Espinoza, and K. C. Pattnayak, 2018: Recent intensification of Amazon flooding extremes driven by strengthened Walker circulation. *Sci. Adv.*, **4**, eaat8785, https://doi.org/10.1126/sciadv.aat8785.

Barlow, J., E. Berenguer, R. Carmenta, and F. França, 2020: Clarifying Amazonia's burning crisis. *Global Change Biol.*, **26**, 319–321, https://doi.org/10.1111/gcb.14872.

Bettolli, M. L., O. C. Penalba, and W. M. Vargas, 2010: Synoptic weather types in the south of South America and their relationship to daily precipitation in the core production region of crops in Argentina. *Aust. Meteor. Oceanogr. J.*, **60**, 37–48, https://doi.org/10.22499/2.6001.004.

Boisier, J. P., P. Ciais, A. Ducharne, and M. Guimberteau, 2015: Projected strengthening of Amazonian dry season by constrained climate model simulations. *Nat. Climate Change*, **5**, 656–660, https://doi.org/10.1038/nclimate2658.

Brando, P. M., and Coauthors, 2014: Abrupt increases in Amazonian tree mortality due to drought fire interactions. *Proc. Natl. Acad. Sci. USA*, **111**, 6347–6352, https://doi.org/10.1073/pnas.1305499111.

Brienen, R. J. W., and Coauthors, 2015: Long-term decline of the Amazon carbon sink. *Nature*, **519**, 344–348, https://doi.org/10.1038/nature14283.

Butt, N., P. A. de Oliveira, and M. H. Costa, 2011: Evidence that deforestation affects the onset of the rainy season in Rondonia, Brazil. *J. Geophys. Res.*, **116**, D11120, https://doi.org/10.1029/2010JD015174.

Calinski, T., and J. Harabasz, 1974: A dendrite method for cluster analysis. *Commun. Stat.*, **3**, 1–27, https://doi.org/10.1080/03610927408827101.

Carvalho, L., C. Jones, and B. Liebmann, 2004: The South Atlantic convergence zone: Intensity, form, persistence, and relationships with intraseasonal to interannual activity and extreme rainfall. *J. Climate*, **17**, 88–108, https://doi.org/10.1175/1520-0442(2004)017<0088:TSACZI>2.0.CO;2.

Cavalcante, R. B. L., D. B. da Silva Ferreira, P. R. M. Pontes, R. G. Tedeschi, C. P. W. da Costa, and E. B. de Souza, 2020: Evaluation of extreme rainfall indices from CHIRPS precipitation estimates over the Brazilian Amazonia. *Atmos. Res.*, **238**, 104879, https://doi.org/10.1016/j.atmosres.2020.104879.

Chen, Y., D. C. Morton, N. Andela, G. R. van der Werf, L. Giglio, and J. T. Randerson, 2017: A pan-tropical cascade of fire driven by El Niño/Southern Oscillation. *Nat. Climate Change*, **7**, 906–911, https://doi.org/10.1038/s41558-017-0014-8.

Conciani, D. E., L. P. dos Santos, T. S. F. Silva, G. Durigan, and S. T. Alvarado, 2021: Human–climate interactions shape fire regimes in the Cerrado of São Paulo state, Brazil. *J. Nat. Conserv.*, **61**, 126006, https://doi.org/10.1016/j.jnc.2021.126006.

Cook, B. I., J. S. Mankin, K. Marvel, A. P. Williams, J. E. Smerdon, and K. J. Anchukaitis, 2020: Twenty-first century drought projections in the CMIP6 forcing scenarios. *Earth's Future*, **8**, e2019EF001461, https://doi.org/10.1029/2019EF001461.

Correa, I., P. A. Arias, and M. Rojas, 2021: Evaluation of multiple indices of the South American monsoon. *Int. J. Climatol.*, **41**, E2801–E2819, https://doi.org/10.1002/joc.6880.

Cunha, A. P. M. A., and Coauthors, 2019: Extreme drought events over Brazil from 2011 to 2019. *Atmosphere*, **10**, 642, https://doi.org/10.3390/atmos10110642.

da Anunciação, Y. M. T., D. H. G. Walde, and R. P. da Rocha, 2014: Observed summer weather regimes and associated extreme precipitation over Distrito Federal, west-central Brazil. *Environ. Earth Sci.*, **72**, 4835–4848, https://doi.org/10.1007/s12665-014-3607-9.

da Silva, A. E., and L. M. V. de Carvalho, 2007: Large-scale index for South America monsoon (LISAM). *Atmos. Sci. Lett.*, **8**, 51–57, https://doi.org/10.1002/asl.150.

da Silva, C. A., Jr., and Coauthors, 2020: Persistent fire foci in all biomes undermine the Paris agreement in Brazil. *Sci. Rep.*, **10**, 16246, https://doi.org/10.1038/s41598-020-72571-w.

Debortoli, N., V. Dubreuil, B. Funatsu, F. Delahaye, C. H. de Oliveira, S. Rodrigues-Filho, C. H. Saito, and R. Fetter, 2015: Rainfall patterns in the southern Amazon: A chronological perspective (1970–2010). *Climatic Change*, **130**, 251–264, https://doi.org/10.1007/s10584-015-1415-1.

Diday, E., and J. C. Simon, 1976: Clustering analysis. *Digital Pattern Recognition*, K. S. Fu, Ed., Springer, 47–94.

Doelling, D. R., and Coauthors, 2013: Geostationary enhanced temporal interpolation for CERES flux products. *J. Atmos. Oceanic Technol.*, **30**, 1072–1090, https://doi.org/10.1175/JTECH-D-12-00136.1.

——, M. Sun, L. T. Nguyen, M. L. Nordeen, C. O. Haney, D. F. Keyes, and P. E. Mlynczak, 2016: Advances in geostationary-derived longwave fluxes for the CERES synoptic (SYN1deg) product. *J. Atmos. Oceanic Technol.*, **33**, 503–521, https://doi.org/10.1175/JTECH-D-15-0147.1.

Espinoza, J. C., and Coauthors, 2009: Spatio-temporal rainfall variability in the Amazon basin countries (Brazil, Peru, Bolivia, Colombia, and Ecuador). *Int. J. Climatol.*, **29**, 1574–1594, https://doi.org/10.1002/joc.1791.

——, J. Ronchail, J. L. Guyot, C. Junquas, P. Vauchel, W. S. Lavado, G. Drapeau, and R. Pombosa, 2011: Climate variability and extremes drought in the upper Solimões River (western Amazon Basin): Understanding the exceptional 2010 drought. *Geophys. Res. Lett.*, **38**, L13406, https://doi.org/10.1029/2011GL047862.

——, M. Lengaigne, J. Ronchail, and S. Janicot, 2012: Large-scale circulation patterns and related rainfall in the Amazon Basin: A neuronal networks approach. *Climate Dyn.*, **38**, 121–140, https://doi.org/10.1007/s00382-011-1010-8.

——, J. Ronchail, M. Lengaigne, N. Quispe, Y. Silva, M. L. Bettolli, G. Avalos, and A. Llacza, 2013: Revisiting wintertime cold air intrusions at the east of the Andes: Propagating features from subtropical Argentina to Peruvian Amazon and relationship with large-scale circulation patterns. *Climate Dyn.*, **41**, 1983–2002, https://doi.org/10.1007/s00382-012-1639-y.

——, S. Chavez, J. Ronchail, C. Junquas, K. Takahashi, and W. Lavado, 2015: Rainfall hotspots over the southern tropical Andes: Spatial distribution, rainfall intensity, and relations with large-scale atmospheric circulation. *Water Resour. Res.*, **51**, 3459–3475, https://doi.org/10.1002/2014WR016273.

——, H. Segura, J. Ronchail, G. Drapeau, and O. Gutierrez-Cori, 2016: Evolution of wet-day and dry-day frequency in the western Amazon basin: Relationship with atmospheric circulation and impacts on vegetation. *Water Resour. Res.*, **52**, 8546–8560, https://doi.org/10.1002/2016WR019305.

——, J. Ronchail, J. A. Marengo, and H. Segura, 2019a: Contrasting north–south changes in Amazon wet-day and dry-day frequency and related atmospheric features (1981–2017). *Climate Dyn.*, **116**, 5413–5430, https://doi.org/10.1007/s00382-018-4462-2.

——, and Coauthors, 2019b: Regional hydro-climatic changes in the southern Amazon basin (upper Madeira basin) during the 1982–2017 period. *J. Hydrol. Reg. Stud.*, **26**, 100637, https://doi.org/10.1016/j.ejrh.2019.100637.

——, R. Garreaud, G. Poveda, P. A. Arias, J. Molina-Carpio, M. Masiokas, M. Viale, and L. Scaff, 2020: Hydroclimate of the Andes part I: Main climatic features. *Front. Earth Sci.*, **8**, 64, https://doi.org/10.3389/feart.2020.00064.

Fernandes, K., and Coauthors, 2011: North tropical Atlantic influence on western Amazon fire season variability. *Geophys. Res. Lett.*, **38**, L12701, https://doi.org/10.1029/2011GL047392.

Figueroa, M., E. Armijos, J. C. Espinoza, J. Ronchail, and P. Fraizy, 2020: On the relationship between reversal of the river stage (*repiquetes*), rainfall and low-level wind regimes over the western Amazon basin. *J. Hydrol.*, **32**, 100752, https://doi.org/10.1016/j.ejrh.2020.100752.

Fu, R., and W. Li, 2004: The influence of the land surface on the transition from dry to wet season in Amazonia. *Theor. Appl. Climatol.*, **78**, 97–110, https://doi.org/10.1007/s00704-004-0046-7.

——, B. Zhu, and R. E. Dickinson, 1999: How do atmosphere and land surface influence seasonal changes of convection in the tropical Amazon? *J. Climate*, **12**, 1306–1321, https://doi.org/10.1175/1520-0442(1999)012<1306:HDAALS>2.0.CO;2.

——, and Coauthors, 2013: Increased dry season length over southern Amazonia in recent decades and its implication for future climate projection. *Proc. Natl. Acad. Sci. USA*, **110**, 18 110–18 115, https://doi.org/10.1073/pnas.1302584110.

Funatsu, B. M., R. Le Roux, D. Arvor, J. C. Espinoza, C. Claud, J. Ronchail, V. Michot, and V. Dubreuil, 2021: Assessing precipitation extremes (1981–2018) and deep convective activity (2002–2018) in the Amazon region with CHIRPS and AMSU data. *Climate Dyn.*, **57**, 827–849, https://doi.org/10.1007/s00382-021-05742-8.

Funk, C., and Coauthors, 2015: The Climate Hazards Infrared Precipitation with Stations—A new environmental record for monitoring extremes. *Sci. Data*, **2**, 150066, https://doi.org/10.1038/sdata.2015.66.

Gan, M. A., V. E. Kousky, and C. F. Ropelewski, 2004: The South America monsoon circulation and its relationship to rainfall over west-central Brazil. *J. Climate*, **17**, 47–66, https://doi.org/10.1175/1520-0442(2004)017<0047:TSAMCA>2.0.CO;2.

Garreaud, R. D., 2000: Cold air incursions over subtropical South America: Mean structure and dynamics. *Mon. Wea. Rev.*, **128**, 2544–2559, https://doi.org/10.1175/1520-0493(2000)128<2544:CAIOSS>2.0.CO;2.

——, 2009: The Andes climate and weather. *Adv. Geosci.*, **22**, 3–11, https://doi.org/10.5194/adgeo-22-3-2009.

——, M. Vuille, and A. Clement, 2003: The climate of the Altiplano: Observed current conditions and mechanisms of past changes. *Palaeogeogr. Palaeoclimatol. Palaeoecol.*, **194**, 5–22, https://doi.org/10.1016/S0031-0182(03)00269-4.

——, ——, R. Compagnucci, and J. Marengo, 2009: Present-day South American climate. *Palaeogeogr. Palaeoclimatol. Palaeoecol.*, **281**, 180–195, https://doi.org/10.1016/j.palaeo.2007.10.032.

Ghil, M., and A. W. Robertson, 2002: "Waves" vs. "particles" in the atmosphere's phase space: A pathway to long-range forecasting? *Proc. Natl. Acad. Sci. USA*, **99** (Suppl. 1), 2493–2500, https://doi.org/10.1073/pnas.012580899.

Giglio, L., L. Boschetti, D. P. Roy, M. L. Humber, and C. O. Justice, 2018: The Collection 6 MODIS burned area mapping algorithm and product. *Remote Sens. Environ.*, **217**, 72–85, https://doi.org/10.1016/j.rse.2018.08.005.

Giráldez, L., Y. Silva, R. Zubieta, and J. Sulca, 2020: Change of the rainfall seasonality over central Peruvian Andes: Onset, end, duration and its relationship with large-scale atmospheric circulation. *Climate*, **8**, 23, https://doi.org/10.3390/cli8020023.

Gouirand, I., V. Moron, and B. Sing, 2020: Seasonal atmospheric transitions in the Caribbean basin and Central America. *Climate Dyn.*, **55**, 1809–1828, https://doi.org/10.1007/s00382-020-05356-6.

Green, R., S. Bordoni, D. S. Battisti, and K. Hui, 2020: Monsoons, ITCZs, and the concept of the global monsoon. *Rev. Geophys.*, **58**, e2020RG000700, https://doi.org/10.1029/2020RG000700.

Gutierrez-Cori, O., J. C. Espinoza, L. Z. X. Li, S. Wongchuig, P. A. Arias, J. Ronchail, and H. Segura, 2021: On the hydroclimate–vegetation relationship in the southwestern Amazon during the 2000–2019 period. *Front. Water*, **3**, 648499, https://doi.org/10.3389/frwa.2021.648499.

Haghtalab, N., N. Moore, B. P. Heerspink, and D. W. Hyndman, 2020: Evaluating spatial patterns in precipitation trends across the Amazon basin driven by land cover and global scale forcings. *Theor. Appl. Climatol.*, **140**, 411–427, https://doi.org/10.1007/s00704-019-03085-3.

Hersbach, N., and Coauthors, 2020: The ERA5 global reanalysis. *Quart. J. Roy. Meteor. Soc.*, **146**, 1999–2049, https://doi.org/10.1002/qj.3803.

Hewitson, B., and R. Crane, 2002: Self-organizing maps: Applications to synoptic climatology. *Climate Res.*, **22**, 13–26, https://doi.org/10.3354/cr022013.

INPE, 2018: Lançamento da "Base 2" de focos de queima de vegetação (Launch of "Base 2" of vegetation burning outbreaks). Instituto Nacional de Pesquisas Espaciais, https://queimadas.dgi.inpe.br/queimadas/portal/informacoes/novidades/lancamento-da-colecao-2-de-dados-de-focos-de-calor.

Jimenez, J. C., J. A. Marengo, L. M. Alves, J. C. Sulca, K. Takahashi, S. Ferrett, and M. Collins, 2021: The role of ENSO flavours and TNA on recent droughts over Amazon forests and the Northeast Brazil region. *Int. J. Climatol.*, **41**, 3761–3780, https://doi.org/10.1002/joc.6453.

Kousky, V. E., 1988: Pentad outgoing longwave radiation climatology for the South American sector. *Rev. Bras. Meteor.*, **3**, 217–231.

Leite-Filho, A. T., V. Y. de Sousa Pontes, and M. H. Costa, 2019: Effects of deforestation on the onset of the rainy season and the duration of dry spells in southern Amazonia. *J. Geophys. Res. Atmos.*, **124**, 5268–5281, https://doi.org/10.1029/2018JD029537.

Lenters, J.-D., and K.-H. Cook, 1997: On the origin of the Bolivian high and related circulation features of the South American climate. *J. Atmos. Sci.*, **54**, 656–678, https://doi.org/10.1175/1520-0469(1997)054<0656:OTOOTB>2.0.CO;2.

Li, W., and R. Fu, 2004: Transition of the large-scale atmospheric and land surface conditions from the dry to the wet season over Amazonia as diagnosed by the ECMWF re-analysis. *J. Climate*, **17**, 2637–2651, https://doi.org/10.1175/1520-0442(2004)017<2637:TOTLAA>2.0.CO;2.

——, and ——, 2006: Influence of cold air intrusions on the wet season onset over Amazonia. *J. Climate*, **19**, 257–275, https://doi.org/10.1175/JCLI3614.1.

Libonati, R., and Coauthors, 2021: Twenty-first century droughts have not increasingly exacerbated fire season severity in the Brazilian Amazon. *Sci. Rep.*, **11**, 4400, https://doi.org/10.1038/s41598-021-82158-8.

Liebmann, B., and C. A. Smith, 1996: Description of a complete (interpolated) outgoing longwave radiation dataset. *Bull. Amer. Meteor. Soc.*, **77**, 1275–1277, https://doi.org/10.1175/1520-0477-77.6.1274.

——, and J. Marengo, 2001: Interannual variability of the rainy season and rainfall in the Brazilian Amazon basin. *J. Climate*, **14**, 4308–4318, https://doi.org/10.1175/1520-0442(2001)014<4308:IVOTRS>2.0.CO;2.

Lupo, A. R., J. J. Nocera, L. F. Bosart, E. G. Hoffman, and D. J. Knight, 2001: South American cold surges: Types, composites, and case studies. *Mon. Wea. Rev.*, **129**, 1021–1041, https://doi.org/10.1175/1520-0493(2001)129<1021:SACSTC>2.0.CO;2.

Marengo, J. A., and J. C. Espinoza, 2016: Extreme seasonal droughts and floods in Amazonia: Causes, trends and impacts. *Int. J. Climatol.*, **36**, 1033–1050, https://doi.org/10.1002/joc.4420.

——, W. R. Soares, C. Saulo, and M. Nicolini, 2004: Climatology of the low-level jet east of the Andes as derived from NCEP–NCAR reanalyses: Characteristics and temporal variability. *J. Climate*, **17**, 2261–2280, https://doi.org/10.1175/1520-0442(2004)017<2261:COTLJE>2.0.CO;2.

——, J. Tomasella, L. M. Alves, W. R. Soares, and D. A. Rodriguez, 2011: The drought of 2010 in the context of historical droughts in the Amazon region. *Geophys. Res. Lett.*, **38**, L12703, https://doi.org/10.1029/2011GL047436.

——, and Coauthors, 2012: Recent developments on the South American monsoon system. *Int. J. Climatol.*, **32** (1), 1–21, https://doi.org/10.1002/joc.2254.

——, G. F. Fisch, L. M. Alves, N. V. Sousa, R. Fu, and Y. Zhuang, 2017: Meteorological context of the onset and end of the rainy season in Central Amazonia during the GoAmazon2014/5. *Atmos. Chem. Phys.*, **17**, 7671–7681, https://doi.org/10.5194/acp-17-7671-2017.

Mayta, V. C., T. Ambrizzi, J. C. Espinoza, and P. L. Silva Dias, 2018: The role of the Madden–Julian oscillation on the Amazon Basin

intraseasonal rainfall variability. *Int. J. Climatol.*, **39**, 343–360, https://doi.org/10.1002/joc.5810.

Michelangeli, P. A., R. Vautard, and B. Legras, 1995: Weather regimes: Recurrence and quasi stationarity. *J. Atmos. Sci.*, **52**, 1237–1256, https://doi.org/10.1175/1520-0469(1995)052<1237:WRRAQS>2.0.CO;2.

Moon, S., and K.-J. Ha, 2020: Future changes in monsoon duration and precipitation using CMIP6. *npj Climate Atmos. Sci.*, **3**, 45, https://doi.org/10.1038/s41612-020-00151-w.

Moron, V., A. W. Robertson, M.-N. Ward, and O. Ndiaye, 2008: Weather types and rainfall over Senegal. Part I: Observational analysis. *J. Climate*, **21**, 266–287, https://doi.org/10.1175/2007JCLI1601.1.

——, ——, and J. H. Qian, 2010: Local versus regional scale characteristics of monsoon onset and post-onset rainfall over Indonesia. *Climate Dyn.*, **34**, 281–299, https://doi.org/10.1007/s00382-009-0547-2.

——, ——, ——, and M. Ghil, 2015: Weather types across the Maritime Continent: From the diurnal cycle of interannual variations. *Front. Environ. Sci.*, **2**, 65, https://doi.org/10.3389/fenvs.2014.00065.

——, I. Gouirand, and M. Taylor, 2016: Weather types across the Caribbean basin and their relationship with rainfall and sea surface temperature. *Climate Dyn.*, **47**, 601–621, https://doi.org/10.1007/s00382-015-2858-9.

Nobre, C. A., G. Sampaio, L. S. Borma, J. C. Castilla-Rubio, J. S. Silva, and M. Cardoso, 2016: Land-use and climate change risks in the Amazon and the need of a novel sustainable development paradigm. *Proc. Natl. Acad. Sci. USA*, **113**, 10 759–10 768, https://doi.org/10.1073/pnas.1605516113.

Nogués-Paegle, J., and K. Mo, 1997: Alternating wet and dry conditions over South America during summer. *Mon. Wea. Rev.*, **125**, 279–291, https://doi.org/10.1175/1520-0493(1997)125<0279:AWADCO>2.0.CO;2.

Paca, V. H. M., G. E. Espinoza-Dávalos, D. M. Moreira, and G. Comair, 2020: Variability of trends in precipitation across the Amazon River basin determined from the CHIRPS precipitation product and from station records. *Water*, **12**, 1244, https://doi.org/10.3390/w12051244.

Paccini, L., J. C. Espinoza, J. Ronchail, and H. Segura, 2018: Intraseasonal rainfall variability in the Amazon basin related to large-scale circulation patterns: A focus on western Amazon–Andes transition region. *Int. J. Climatol.*, **38**, 2386–2399, https://doi.org/10.1002/joc.5341.

Parsons, L. A., 2020: Implications of CMIP6 projected drying trends for 21st century Amazonian drought risk. *Earth's Future*, **8**, e2020EF001608, https://doi.org/10.1029/2020EF001608.

Ruiz-Vásquez, M., P. A. Arias, J. A. Martínez, and J. C. Espinoza, 2020: Effects of Amazon basin deforestation on regional atmospheric circulation and water vapor transport towards tropical South America. *Climate Dyn.*, **54**, 4169–4189, https://doi.org/10.1007/s00382-020-05223-4.

Sáenz, F., and A. M. Durán-Quesada, 2015: A climatology of low level wind regimes over Central America using a weather type classification approach. *Front Earth Sci.*, **3**, 15, https://doi.org/10.3389/feart.2015.00015.

Segura, H., C. Junquas, J. C. Espinoza, M. Vuille, Y. R. Jauregui, A. Rabatel, T. Condom, and T. Lebel, 2019: New insights into the rainfall variability in the tropical Andes on seasonal and interannual time scales. *Climate Dyn.*, **53**, 405–426, https://doi.org/10.1007/s00382-018-4590-8.

——, J. C. Espinoza, C. Junquas, T. Lebel, M. Vuille, and R. Garreaud, 2020: Recent changes in the precipitation-driving processes over the southern tropical Andes/western Amazon. *Climate Dyn.*, **54**, 2613–2631, https://doi.org/10.1007/s00382-020-05132-6.

Sena, A. C. T., and G. Magnusdottir, 2020: Projected end-of-century changes in the South American monsoon in the CESM large ensemble. *J. Climate*, **33**, 7859–7874, https://doi.org/10.1175/JCLI-D-19-0645.1.

Silva Dias, P. L., W. H. Schubert, and M. De Maria, 1983: Large-scale response of the tropical atmosphere to transient convection. *J. Atmos. Sci.*, **40**, 2689–2707, https://doi.org/10.1175/1520-0469(1983)040<2689:LSROTT>2.0.CO;2.

Solman, S., and C. Menéndez, 2003: Weather regimes in the South American sector and neighbouring oceans during winter. *Climate Dyn.*, **21**, 91–104, https://doi.org/10.1007/s00382-003-0320-x.

Staal, A., O. Tuinenburg, J. Bosmans, and S. C. Dekker, 2018: Forest-rainfall cascades buffer against drought across the Amazon. *Nat. Climate Change*, **8**, 539–543, https://doi.org/10.1038/s41558-018-0177-y.

——, B. M. Flores, A. P. A. Aguiar, J. H. C. Bosmans, I. Fetzer, and O. A. Tuinenburg, 2020: Feedback between drought and deforestation in the Amazon. *Environ. Res. Lett.*, **15**, 044024, https://doi.org/10.1088/1748-9326/ab738e.

Straus, D. M., and F. Molteni, 2004: Flow regimes, SST forcing, and climate noise: Results from large GCM ensembles. *J. Climate*, **17**, 1641–1656, https://doi.org/10.1175/1520-0442(2004)017<1641:CRASFR>2.0.CO;2.

van der Werf, G. R., J. T. Randerson, L. Giglio, N. Gobron, and A. J. Dolman, 2008: Climate controls on the variability of fires in the tropics and subtropics. *Global Biogeochem. Cycles*, **22**, GB3028, https://doi.org/10.1029/2007GB003122.

Vera, C., W. Higgins, J. Amador, T. Ambrizzi, R. Garreaud, and D. Gochis, 2006: Toward a unified view of the American monsoon systems. *J. Climate*, **19**, 4977–5000, https://doi.org/10.1175/JCLI3896.1.

Wang, H., and R. Fu, 2002: Cross-equatorial flow and seasonal cycle of precipitation over South America. *J. Climate*, **15**, 1591–1608, https://doi.org/10.1175/1520-0442(2002)015<1591:CEFASC>2.0.CO;2.

Wielicki, B. A., B. R. Barkstrom, E. F. Harrison, R. B. Lee III, G. L. Smith, and J. E. Cooper, 1996: Clouds and the Earth's Radiant Energy System (CERES): An Earth observing system experiment. *Bull. Amer. Meteor. Soc.*, **77**, 853–868, https://doi.org/10.1175/1520-0477(1996)077<0853:CATERE>2.0.CO;2.

Wilks, D. S., 2006: *Statistical Methods in the Atmospheric Sciences*. Academic Press, 648 pp.

Wright, J. S., R. Fu, J. R. Worden, S. Chakraborty, N. E. Clinton, C. Risi, Y. Sun, and L. Yin, 2017: Rainforest-initiated wet season onset over the southern Amazon. *Proc. Natl. Acad. Sci. USA*, **114**, 8481–8486, https://doi.org/10.1073/pnas.1621516114.

Xu, K. M., T. Wong, S. Dong, F. Chen, S. Kato, and P. C. Taylor, 2016: Cloud object analysis of CERES *Aqua* observations of tropical and subtropical cloud regimes: Four-year climatology. *J. Climate*, **29**, 1617–1638, https://doi.org/10.1175/JCLI-D-14-00836.1.

Yin, L., R. Fu, Y. Zhang, P. A. Arias, N. Fernando, W. Li, K. Fernandes, and A. Bowerman, 2014: What controls interannual variations of the wet season onsets over the Amazon? *J. Geophys. Res. Atmos.*, **119**, 2314–2328, https://doi.org/10.1002/2013JD021349.

Yoon, J.-H., Zeng, N., 2010: An Atlantic influence on Amazon rainfall. *Climate Dyn.* **34**, 249–264, https://doi.org/10.1007/s00382-009-0551-6..

Zemp, D. C., and Coauthors, 2017: Self-amplified Amazon forest loss due to vegetation–atmosphere feedbacks. *Nat. Commun.*, **8**, 14681, https://doi.org/10.1038/ncomms14681.

Zhou, J., and K. M. Lau, 1998: Does a monsoon climate exist over South America? *J. Climate*, **11**, 1020–1040, https://doi.org/10.1175/1520-0442(1998)011<1020:DAMCEO>2.0.CO;2.